PAPER • OPEN ACCESS

Gyrokinetic modelling of the Alfvén mode activity in ASDEX Upgrade with an isotropic slowing-down fast-particle distribution

To cite this article: F. Vannini *et al* 2022 *Nucl. Fusion* **62** 126042

OPEN ACCESS
IOP Publishing | International Atomic Energy Agency Nuclear Fusion
Nucl. Fusion **62** (2022) 126042 (19pp) https://doi.org/10.1088/1741-4326/ac8b1e

Gyrokinetic modelling of the Alfvén mode activity in ASDEX Upgrade with an isotropic slowing-down fast-particle distribution

F. Vannini[1,*], A. Biancalani[2], A. Bottino[1], T. Hayward-Schneider[1], P. Lauber[1], A. Mishchenko[3], E. Poli[1], B. Rettino[1], G. Vlad[4], X. Wang[1] and the ASDEX Upgrade Team[a]

[1] Max-Planck-Institut für Plasmaphysik, Boltzmannstr. 2, 85748 Garching, Germany
[2] Léonard de Vinci Pôle Universitaire, Research Center, 92916 Paris La Défense, France
[3] Max-Planck-Institut für Plasmaphysik, Wendelsteinstraße 1, 17491 Greifswald, Germany
[4] ENEA, FSN, C. R. Frascati, Via E. Fermi 45, 00044 Frascati (Roma), Italy

E-mail: francesco.vannini@ipp.mpg.de

Received 18 February 2022, revised 19 July 2022
Accepted for publication 19 August 2022
Published 8 November 2022

Abstract

In the present paper, the evolution of the Alfvén modes (AMs) is studied in a realistic ASDEX Upgrade equilibrium by analyzing the results of simulations with the global, electromagnetic, gyrokinetic particle-in-cell code ORB5. The energetic particles (EPs) are modelled both via the newly implemented isotropic slowing-down and with Maxwellian distribution functions. The comparison of the numerical results shows that modelling the EPs with the equivalent Maxwellian rather than with the slowing-down, does not significantly affect the frequency of the driven AM, while its growth rate appears to be underestimated with a quantitative difference as large as almost 30%. Additionally the choice of the isotropic slowing-down allows a better description of the nonlinear modification of the dominant AM frequency, while an equivalent Maxwellian underestimates it. A good comparison with the experimental spectrogram is found.

Keywords: Alfvén instabilities, ASDEX Upgrade, isotropic slowing-down, equivalent Maxwellian, TAE, EPM

(Some figures may appear in colour only in the online journal)

1. Introduction

Next-generation fusion machines like ITER [1] and DEMO [2] will be characterized by a significant population of energetic particles (EPs). With this term we refer to fast ions in general that are going to be present in the confining machines as fusion products (α-particles, $_2$He) or as products of auxiliary heating sources like neutral beam injection or ion cyclotron resonance heating. The typical EP velocity v_{EP} is intermediate between the thermal bulk ions velocity $v_{\mathrm{th,i}}$ and the thermal electron velocity $v_{\mathrm{th,e}}$. EPs' gyroradius ρ_{EP} is instead much larger than the bulk plasma species gyroradii (ρ_{i} and ρ_{e}) [3]:

$$v_{\mathrm{th,\,i}} \ll v_{\mathrm{EP}} \ll v_{\mathrm{th,\,e}}, \quad \rho_{\mathrm{EP}} \gg \rho_{\mathrm{i}} \gg \rho_{\mathrm{e}}. \tag{1}$$

Typically in Tokamak machines the EPs' characteristic dynamical frequencies ω associated with their guiding-center motion (transit, bounce and precessional) fall inside the magnetohydrodynamic (MHD) regime $\omega \sim 10^{-2}\omega_{\mathrm{ci}}$, with ω_{ci} the

* Author to whom any correspondence should be addressed.

[a] See Meyer *et al* 2019 (https://doi.org/10.1088/1741-4326/ab18b8) for the ASDEX Upgrade Team.

ion cyclotron frequency. Because of this EPs can resonate with MHD instabilities driving them unstable. Among the MHD instabilities, the most detrimental and easily excited are the nearly incompressible shear Alfvén wave (SAWs). These are transverse electromagnetic waves that propagate along the magnetic field lines with group velocity equal to the Alfvén speed v_{A}. Their dispersion relation is [4, 5]:

$$\omega_{\mathrm{SAW}} = k_{\parallel} v_{\mathrm{A}}, \quad k_{\parallel} = \vec{k} \cdot \hat{\boldsymbol{b}}, \quad v_{\mathrm{A}} = \frac{B_0}{\sqrt{4\pi\rho_{m,0}}}, \tag{2}$$

with $\hat{\boldsymbol{b}} = \boldsymbol{B}_0/B_0$ a unit vector pointing in the direction of the background magnetic field $\boldsymbol{B}_0$ with modulus B_0, $\rho_{m,0}$ the plasma mass density and $\boldsymbol{k}$ the wave-number of the perturbation. In a straight cylinder [6–8]:

$$k_{\parallel} = \frac{1}{R_0}\left(n - \frac{m}{q(r)}\right), \tag{3}$$

with $q(r)$ the safety factor profile, R_0 the major radius of the Tokamak and m and n the poloidal and toroidal mode numbers respectively. SAWs are characterized by a frequency spectrum that varies continuously across the radial domain because of the radial dependence contained in both the Alfvén speed and the safety factor profile.

Different kinds of Alfvén instabilities, that we call for simplicity Alfvén modes (AMs) [9–11], can be present in Tokamak machines. These include both energetic-particle continuum modes (EPMs) [12] and Alfvén eigenmodes (AEs) [10].

EPMs represent forced oscillations of the SAW continuum that arise when the EP pressure is comparable to that of the bulk plasma. They emerge as discrete oscillations at the frequency of the continuum where the wave-EP power exchange is maximized, above the threshold of the continuum damping.

The AEs, on the other hand, are normal modes of the bulk plasma that can be classified into two types. The first type includes modes that arise in correspondence of the radial position r_0 where different branches of the continuum, see equation (3), cross. There two counterpropagating waves interfere destructively, opening a gap in the continuum where modes reside. An important example of gap modes is represented by the toroidal Alfvén eigenmodes (TAEs [5, 13–15]) that arise because of the coupling between modes with close poloidal harmonics: (m_0, n) and $(m_0 + 1, n)$. The second type of AEs arise in correspondence of an extremum of the continuum spectrum. There $\partial\omega/\partial r$ vanishes and an effective potential well is established that traps the wave. An example of these kind of modes is represented by the reversed shear Alfvén eigenmodes [16, 17] that are present in correspondence of a minimum in the safety factor profile.

The interest connected with the study of the driven AMs relies on their potentially detrimental role. In fact the driven AMs can interact with the EPs redistributing them in phase-space, enhancing the EP transport. In this way EPs can be expelled before they can thermalize with the bulk plasma leading to a less effective heating [18–20]. Additionally AMs are held responsible for the presence of the so-called abrupt-large-events [21–24]. These are violent and rapid variations of the fluctuating magnetic field in correspondence of which an intense migration of EPs from the core to the periphery is observed, representing a possible threat for the safety of the machine. Therefore, the study of the AM dynamics is of primary importance both for the safety of the machine and because only a small fraction of EP losses can be tolerated to achieve ignition. That is why it is mandatory to gain the necessary insight in the AM dynamics to become predictive about the scenarios that will be met in ITER and DEMO.

In this paper we want to contribute to this task studying the AM dynamics with the code ORB5 [25] in numerical simulations where the so-called 'NLED-AUG case' [26] is considered. With this term we refer to the plasma conditions of the ASDEX Upgrade (AUG) discharge #31213 at time $t = 0.84$ s. The uniqueness of this scenario relies on the fact that it has been obtained by tuning the plasma parameters so that the EPs injected through a neutral beam (NB) have an energy with respect to the bulk plasma temperature $\mathcal{E}_{\mathrm{EP}}/T_{\mathrm{Bulk}} \sim 10^2$ and an induced fast-ion β comparable to that of the bulk plasma. In such a way there is a strong Alfvén activity, the stabilizing effects of the bulk plasma being minimized. In particular, TAE–EPM bursts are observed in correspondence of which energetic particle driven geodesic acoustic modes (EGAMs [27]) appear exhibiting the typical chirping.

Studies of the AM activity with the numerical tool ORB5 [25] using the NLED-AUG scenario have already been presented in references [28, 29]. There the EPs have been modelled, respectively, with Maxwellian distribution functions and with bi-shifted Maxwellians (also known as 'double-bump-on-tail'). These were the two kinds of equilibrium distribution functions available at that time in ORB5 and the choice of one over the other was motivated by the kind of physics we were interested to reproduce. In particular the double-bump-on-tail was chosen because of the need to have an anisotropy in velocity space to drive unstable an EGAM and study its interaction with the AMs. In the works already published a good qualitative comparison with the experiments has been obtained. In this work we want to make a further step showing that, through the slowing-down distribution function [30] newly implemented in ORB5 we are able to go closer to the experimental conditions obtaining an even better quantitative comparison with the experiment.

The present paper is structured as follows. In section 2 the main features and the model of ORB5 are described. In section 3 the NLED-AUG case is briefly described. In section 4 an analytical derivation of the slowing-down distribution function together with details about its implementation in ORB5 are provided. In section 5 the results of numerical simulations obtained taking into account the NLED-AUG case are described. Finally in section 6 the conclusions of this paper are presented.

2. The numerical model

ORB5 [25] is a nonlinear, global, electromagnetic, gyrokinetic, particle-in-cell code that can take into account collisions and sources (neglected in this work).

The code uses a system of straight-field line coordinates: (r, θ^*, φ). As radial coordinate the code takes into account the square root of the poloidal flux ψ normalized at its value at the edge ψ_0: $r = \sqrt{\psi/\psi_0}$ with $0 \leqslant r \leqslant 1$ that labels the magnetic surfaces. φ is the toroidal angular coordinate and θ^* is the poloidal magnetic angle:

$$\theta^* = \frac{1}{2\,q(r)} \int_0^{2\pi} \mathrm{d}\theta' \, \frac{\boldsymbol{B}_0 \cdot \nabla\varphi}{\boldsymbol{B}_0 \cdot \nabla\theta'}, \quad 0 \leqslant \theta^* \leqslant 2\pi \tag{4}$$

with θ' the geometric poloidal angle and $q(r)$ the safety factor profile.

In ORB5 all the physical quantities are normalized with respect to reference parameters. The masses of the considered particle species m_{sp} are given in units of the mass of the main bulk ion species m_{i}, the velocities are given in units of the sound velocity c_{s}, the lengths are given in units of the sound Larmor radius ρ_{s} and the time is given in units of the inverse bulk ion cyclotron frequency:

$$\omega_{\mathrm{ci}} = \frac{q_{\mathrm{i}} B_0}{m_{\mathrm{i}} c}, \quad q_{\mathrm{i}} = e\, Z_i \tag{5}$$

with e the electron charge in absolute value and Z_i the atomic number of the main ion species.

The total distribution function of the sp-particle species f_{sp} is divided into a time-independent part (equilibrium or background distribution function, $F_{0,\mathrm{sp}}$) and a time dependent component δf_{sp}, so that $f_{\mathrm{sp}} = F_{0,\mathrm{sp}} + \epsilon_\delta \delta f_{\mathrm{sp}}$ with ϵ_δ a small parameter. Only the time-dependent component is discretized as will be later discussed. The *gyrokinetic Vlasov equation* for the perturbed (time-dependent) distribution function is:

$$\begin{aligned} \frac{\mathrm{d}}{\mathrm{d}t}\delta f_{\mathrm{sp}} = -\dot{\vec{X}} \cdot \frac{\partial F_{0,\mathrm{sp}}}{\partial \vec{X}}\bigg|_{\mathcal{E},\, v_\parallel} - \dot{\mathcal{E}} \frac{\partial F_{0,\mathrm{sp}}}{\partial \mathcal{E}}\bigg|_{\boldsymbol{X},\, v_\parallel} \\ - \dot{v}_\parallel \frac{\partial F_{0,\mathrm{sp}}}{\partial v_\parallel}\bigg|_{\boldsymbol{X},\, \mathcal{E}}, \quad \mathcal{E} = \frac{v_\parallel^2}{2} + \mu B, \quad \mu = \frac{v_\perp^2}{2B} \end{aligned} \tag{6}$$

where $\boldsymbol{X}$ is the gyrocenter position, while $v_\parallel$ and $v_\perp$ are, respectively, the parallel and perpendicular components of the particle velocity. The equation of motions in mixed-variable formulation [31] of the *gyrocenter characteristics* of the particle species are [32]:

$$\begin{aligned} \dot{\vec{X}} = v_\parallel \hat{\boldsymbol{b}}^* + \frac{1}{q_{\mathrm{sp}} B_\parallel^*} \hat{\boldsymbol{b}} \times \mu \nabla B \\ + \epsilon_\delta \left[\frac{\hat{\vec{b}}}{B_\parallel^*} \times \nabla \langle \delta\phi - v_\parallel \delta A_\parallel^h - v_\parallel \delta A_\parallel^s \rangle_\alpha - \frac{q_{\mathrm{sp}}}{m_{\mathrm{sp}}} \langle \delta A_\parallel^h \rangle_\alpha \hat{\vec{b}}^* \right] \end{aligned} \tag{7}$$

$$\dot{v}_\parallel = -\frac{\mu}{m_{\mathrm{sp}}} \hat{\boldsymbol{b}}^* \cdot B - \epsilon_\delta \left\{ \mu \frac{\hat{\vec{b}} \times \nabla B}{B_\parallel^*} \cdot \nabla \langle \delta A_\parallel^s \rangle_\alpha + \frac{q_{\mathrm{sp}}}{m_{\mathrm{sp}}} \left[\hat{\vec{b}}^* \cdot \nabla \langle \delta\phi - v_\parallel \delta A_\parallel^h \rangle_\alpha + \frac{\partial}{\partial t} \langle \delta A_\parallel^s \rangle_\alpha \right] \right\} \tag{8}$$

$$\dot{\mathcal{E}} = v_\parallel \dot{v}_\parallel + \mu \nabla B \cdot \dot{\vec{X}}, \quad \dot{\mu} = 0. \tag{9}$$

In equations (7) to (9), m_{sp} and $q_{\mathrm{sp}} = eZ_{\mathrm{sp}}$ are respectively the mass and charge of the sp-particle species with atomic number Z_{sp}. Note that for the electron species $Z_{\mathrm{e}} = -1$. Still in equations (7) to (9) the gyroaveraging operator appears:

$$\begin{aligned} \langle F \rangle_\alpha &= \frac{1}{2\pi} \int_0^{2\pi} \mathrm{d}\alpha \, F(\boldsymbol{X} + \boldsymbol{\rho}_0) \\ &= \frac{1}{2\pi} \int_0^{2\pi} \mathrm{d}\alpha \int \mathrm{d}^3\boldsymbol{r} \, F(\boldsymbol{r}) \, \delta^3(\boldsymbol{X} + \boldsymbol{\rho}_0 - \boldsymbol{r}) = \mathcal{J}_0^{gc}(F) \end{aligned} \tag{10}$$

that removes the fast gyroangle α dependence into a general quantity F, with $\boldsymbol{\rho}_0(\boldsymbol{X}, \alpha)$ the gyroradius. $\delta\phi$ is the perturbed scalar potential and $\delta A_\parallel$ is the perturbed magnetic parallel potential decomposed into symplectic and Hamiltonian parts: $\delta A_\parallel = \delta A_\parallel^h + \delta A_\parallel^s$. $B_\parallel^*$ is the parallel component of the symplectic magnetic field $\boldsymbol{B}^*$, linked to the symplectic magnetic potential $\boldsymbol{A}^*$ by the following relation:

$$\boldsymbol{A}^* = \boldsymbol{A} + \frac{m_{\mathrm{sp}}}{q_{\mathrm{sp}}} v_\parallel \hat{\boldsymbol{b}}, \quad \boldsymbol{B}^* = \nabla \times \boldsymbol{A}^*, \quad \hat{\boldsymbol{b}}^* = \frac{\boldsymbol{B}^*}{B_\parallel^*} = \frac{\boldsymbol{B}^*}{\hat{\boldsymbol{b}} \cdot \boldsymbol{B}^*}. \tag{11}$$

In ORB5 only the perpendicular component of the perturbed magnetic field $\delta\boldsymbol{B}_\perp$ is implemented: $\delta\boldsymbol{B}_\perp = \hat{\boldsymbol{b}} \times \nabla \delta A_\parallel$. In equation (11) $\boldsymbol{A}$ is the background magnetic potential: $\boldsymbol{B}_0 = \nabla \times \boldsymbol{A}$ and $\hat{\boldsymbol{b}}$ a unit vector pointing in the direction of the background magnetic field. The characteristic equations equations (7) to (9) are coupled to the field equations. These are the *gyrokinetic quasi-neutrality equation*:

$$-\nabla \cdot \left[\left(\sum_{\mathrm{sp}=i,f} \frac{q_{\mathrm{sp}}^2 n_{\mathrm{sp}}}{T_{\mathrm{sp}}} \rho_{\mathrm{sp}}^2 \right) \nabla_\perp \delta\phi \right] = \sum_{\mathrm{sp}=i,e,f} q_{\mathrm{sp}} \, \delta n_{\mathrm{sp}}, \qquad \delta n_{\mathrm{sp}} = \int \mathrm{d}W \langle \delta f_{\mathrm{sp}} \rangle \tag{12}$$

the *parallel Ampère's law*

$$\left(\sum_{\mathrm{sp}=i,e,f} \frac{\beta_{\mathrm{sp}}}{\rho_{\mathrm{sp}}^2} - \nabla_\perp^2 \right) \delta A_\parallel^h = \mu_0 \sum_{\mathrm{sp}=i,e,f} \delta j_{\parallel,\mathrm{sp}} + \nabla_\perp^2 \delta A_\parallel^s, \qquad \delta j_{\parallel,\mathrm{sp}} = q_{\mathrm{sp}} \int \mathrm{d}W \, v_\parallel \, \langle \delta f_{\mathrm{s}} \rangle \tag{13}$$

and the *ideal Ohm's law*:

$$\frac{\partial}{\partial t} \delta A_\parallel^s + \hat{\vec{b}} \cdot \nabla \delta\phi = 0 \tag{14}$$

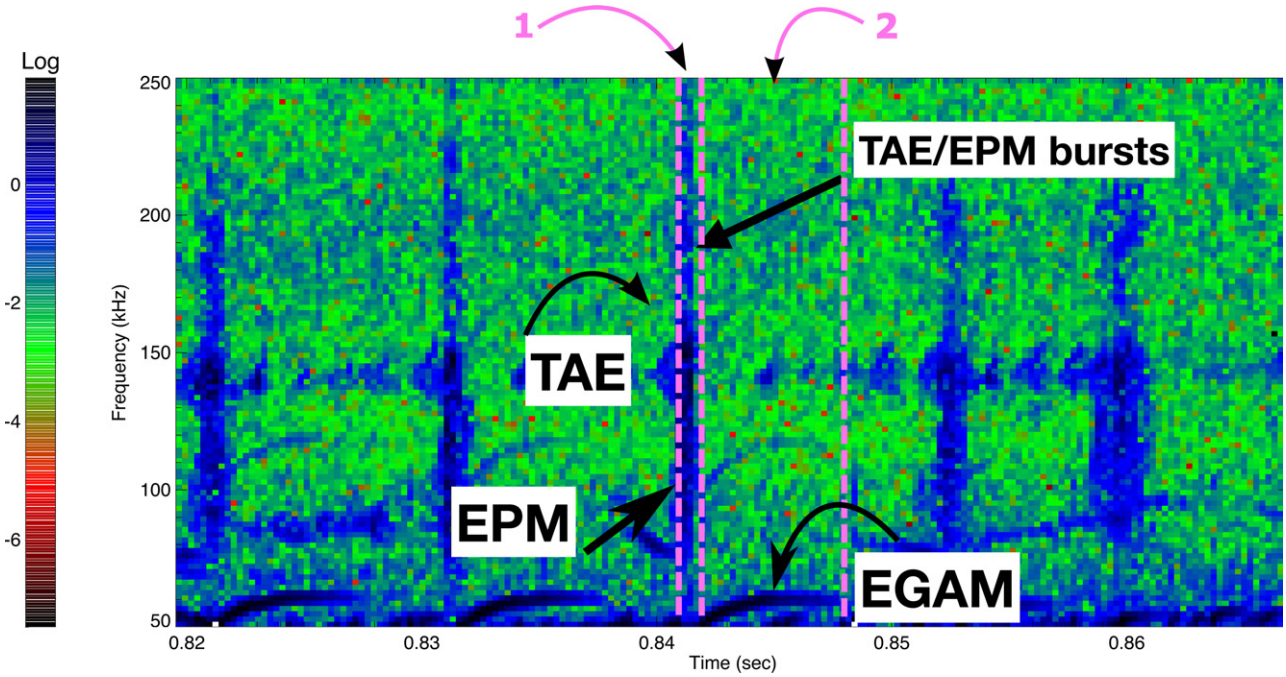

Figure 1. Experimental spectrogram of the magnetic pick-up coil signal. At $t = 0.84$ s the plasma parameters, profiles and the reconstructed magnetic equilibrium have been selected to perform numerical simulations. Regions number 1 and 2 contained between the first and second and the second and third vertical purple dashed lines label, respectively, the temporal domains where the AM ($n = 1$) and the EGAM ($n = 0$) are the most unstable modes.

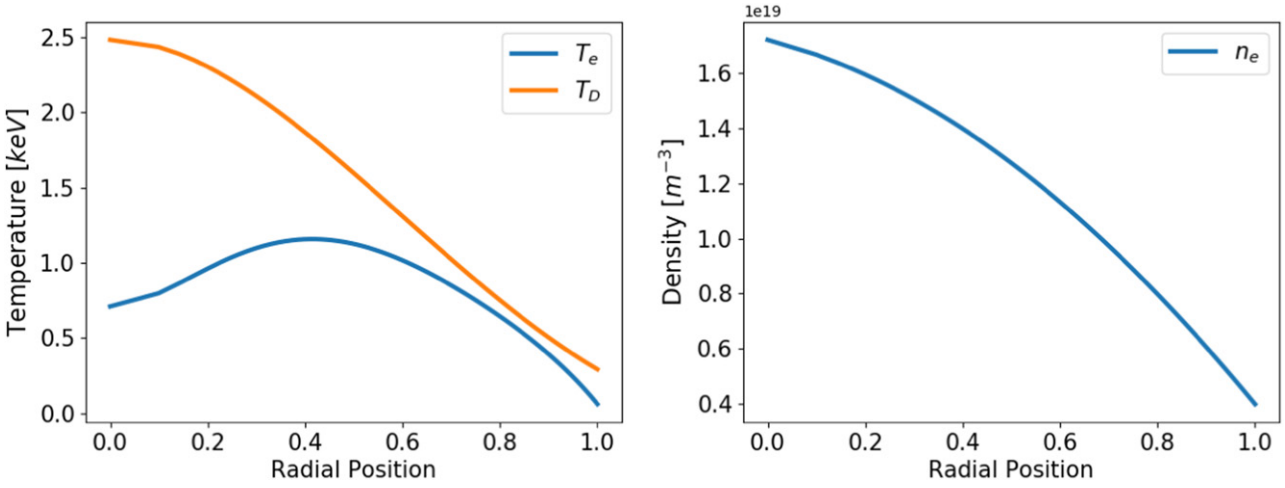

Figure 2. Left: radial temperature profiles of the bulk plasma species (electrons and deuterium) of the NLED-AUG case as modelled by TRANSP. Right: experimental radial electron density profile of the NLED-AUG case.

where:

$$n_{\mathrm{sp}} = \int \mathrm{d}W\, F_{0,\mathrm{sp}}, \quad \beta_{\mathrm{sp}} = \mu_0 \frac{n_{\mathrm{sp}} T_{\mathrm{sp}}}{B_0^2}, \tag{15}$$

where $\mathrm{d}W = B_{\parallel}^{*}\, \mathrm{d}v_{\parallel}\, \mathrm{d}\mu\, \mathrm{d}\alpha$. Equations (6) to (9) and (12) to (14) constitute the gyrokinetic Vlasov–Maxwell system of equations solved by ORB5.

The discretization is achieved sampling the phase-space with a set of super-particles called *markers*. The kth marker of the sp-particle species is associated to a weight $\omega_{\mathrm{sp},k}(t)$. This is a time-dependent quantity that represents at the time t the variation of the number of physical particles contained in a small volume in phase-space Ω_k, centred around the kth marker:

$$\delta N_{\mathrm{sp}}^{\mathrm{physicalparticles}} = \int_{\Omega_k} \mathrm{d}^6\mathbf{Z}\, \delta f_{\mathrm{sp}}(\mathbf{Z}(t), t) = \omega_{\mathrm{sp},k}(t). \tag{16}$$

Each marker is pushed along its orbit slowing the characteristics equations through a Runge–Kutta method at 4th order.

The perturbed fields $\Psi = \{\delta\phi, \delta A_{\parallel}\}$ are discretized using the finite-elements Galerkin approximation. The fields are rep-

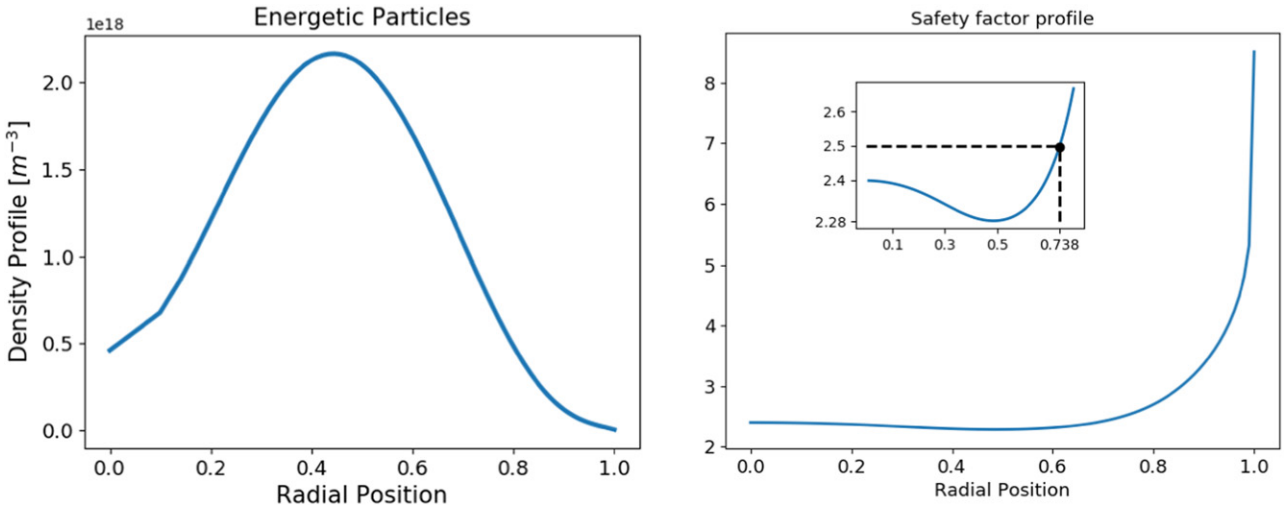

Figure 3. Left: EPs off-axis radial density profile as modelled by TRANSP. It has a reference concentration of $\langle n_{\rm EP}\rangle/\langle n_{\rm e}\rangle = 0.0949$. Right: safety factor profile of the NLED-AUG case. It exhibits a non-monotonic profile with a minimum around $r \approx 0.5$ where $q \approx 2.28$ and a maximum at $r = 1$ in the amount of $q \approx 8.5$. The inset figure marks the TAE location at $r_0 \approx 0.738$, corresponding to the radial position where the following analytical estimate is fulfiled [36]: $q_0 = q(r_0) = (2m_0 + 1)/2 = 2.5$, with $n = 1$ and $m_0 = 2$.

Table 1. Constants in use: averaged minor radius a_0, major radius R_0, amplitude of the background magnetic field on axis B_0. Normalized electron pressure $\beta_{\rm e} = 4\pi\, n_{\rm e}(r_0)T_{\rm e}(r_0)/B_0^2$ with the r_0 a reference radial position. Normalized size of the plasma system that is $L_x = 2a_0/\rho_{\rm s}$, with $\rho_{\rm s} = c_{\rm s}/\omega_{\rm ci}$ and $c_{\rm s}$ the sound velocity and $\omega_{\rm ci}$ the ion cyclotron frequency. $\omega_{\rm A0}$ is the value of the Alfvén frequency on axis.

a_0 (m)	R_0 (m)	B_0 (T)	$\beta_{\rm e}$	L_x	$\omega_{\rm ci}$ (rad s^{-1})	$\omega_{\rm A0}$ (rad s^{-1})	$\omega_{\rm ci}/\omega_{\rm A0}$
0.482	1.666	2.202	$2.7 \cdot 10^{-4}$	551.6	$1.055 \cdot 10^{8}$	$4.98 \cdot 10^{6}$	≈21

resented as linear combinations of finite dimensional function space $\Lambda_\mu(\boldsymbol{x})$:

$$\Psi(\boldsymbol{x}, t) = \sum_\mu \Psi_\mu(t)\Lambda_\mu(\boldsymbol{x}), \tag{17}$$

where the basis $\Lambda_\mu(\boldsymbol{x})$ are tensor product of 1D polynomials (B-splines) of degree $p = 1, 2, 3$:

$$\Lambda_\mu(\boldsymbol{x}) = \Lambda_j^p(r)\Lambda_k^p(\theta^*)\Lambda_l^p(\varphi) \quad \text{with} \quad \mu = (j, k, l). \tag{18}$$

In the present work $p = 3$. The number of B-splines in each direction is connected to the number of grid points (knots) $(N_{\rm r}, N_{\theta^*}, N_\varphi)$ associated to the B-splines and to the chosen degree p of the polynomials. Through the decomposition expressed in equation (17) the fields equations become a set of linear equations to which is applied the double discrete Fourier transformation $\mathcal{F}$ in both the poloidal and toroidal directions. Inverting the obtained system of equations, it is then possible to calculate the Fourier coefficients of the perturbations, to which a Fourier filter is applied. This is given by a field aligned filter:

$$m \in \underbrace{[n\,q(r) - \Delta m, n\,q(r) + \Delta m]}_{\text{field aligned filter}}, \quad n \in [nfilt1, nfilt2]. \tag{19}$$

In equation (19) *nfilt*1, *nfilt*2 are the range boundaries of the rectangular filter for the toroidal coefficients. Δm, instead, is the width of the field aligned filter.

In section 5 results of ORB5 simulations will be discussed. There we will indicate some important parameters used in the

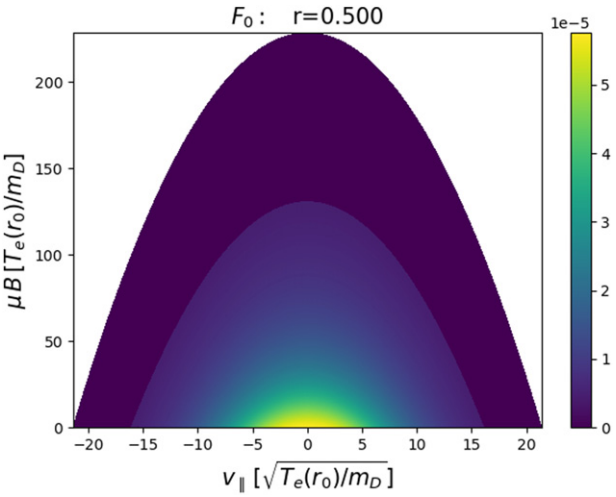

Figure 4. Slowing-down distribution implemented in ORB5 for the EPs. The dependence in velocity-space at a fixed radial position is shown.

simulations. We will specify: the number of grid points associated to the B-splines $(N_{\rm r}, N_{\theta^*}, N_\varphi)$, the number of markers used for every particle species $nptot_{\rm sp}$, the time step in use Δt and the width of the field aligned filter Δm. In this work only the AMs in the NLED-AUG scenario are investigated by retaining, as in previous works [28, 33], only the modes with toroidal mode number equal to one: $nfilt1 = nfilt2 = 1$. Additionally only the EPs will be allowed to redistribute in

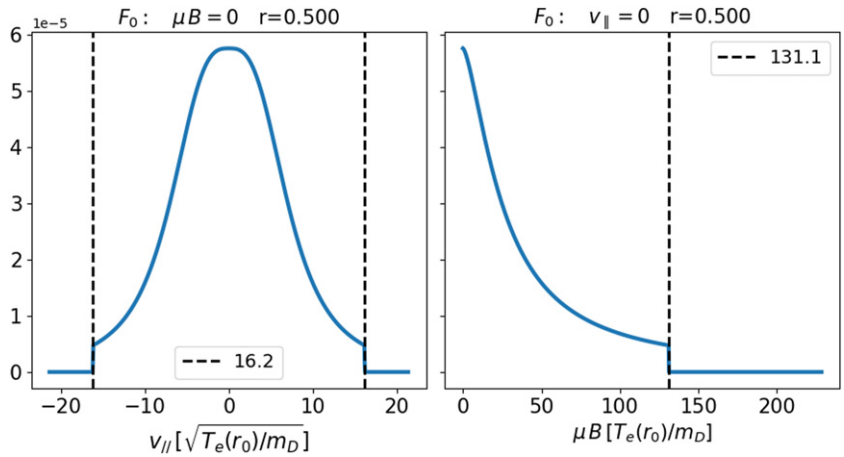

Figure 5. Slices of the equilibrium distribution function obtained from figure 4. Left: dependence against $v_\parallel$: $F_0(r = 0.5, v_\parallel, \mu B = 0)$. Right: dependence against μB: $F_0(r = 0.5, v_\parallel = 0, \mu B)$. The vertical black dashed lines correspond to the cuts in velocity space present because of the Heaviside theta contained in equation (21).

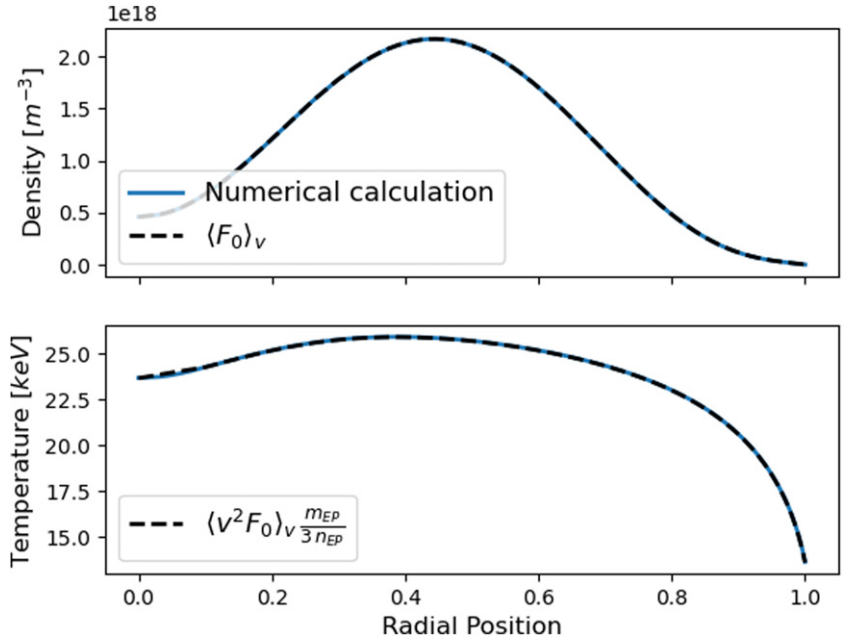

Figure 6. Top: EP radial density profile corresponding to figure 3 left. Bottom: EP equivalent temperature, cf equation (27). $\langle \cdots \rangle_v$ indicates integration in velocity space. The moments of the equilibrium distribution function F_0 implemented in ORB5 and calculated through numerical integration (blue curves) are compared with the expected values (black dashed lines) corresponding, respectively, on the top to figure 3 left and on the bottom to equation (27).

Table 2. Main simulation parameters: time step (Δt), number of markers for particle species (*nptot*). Radial/poloidal/toroidal grid points ($N_r, N_{\theta^*}, N_\varphi$), toroidal (*nfilt*) and poloidal width (Δm) of the field aligned Fourier filter (see section 2).

$\Delta t\,[\omega_{ci}^{-1}]$	$nptot_{D,e,EP} \cdot 10^7$	N_r	N_{θ^*}	N_φ	*nfilt*	Δm
4	3, 12, 3	3000	64	32	1	7

phase-space, following their full trajectories. The bulk plasma species instead will follow their unperturbed trajectories. This means that in equations (7) to (9) the small parameter is taken, with abuse of notation, equal to one only for the EPs while for the electrons and the bulk ions species it is identically zero.

In the following sections we will also specify if a drift-kinetic model is considered and finite-Larmor-radius (FLR) are neglected, or if a gyrokinetic model is considered and FLR effects are taken into account.

3. NLED-AUG scenario

As stated in the introduction, with the term NLED-AUG case [34] we refer to the plasma conditions present at $t = 0.84$ s in the discharge number 31213 (#31213@0.84 s) performed in the Tokamak AUG. EPs, in this experimental case, are due to

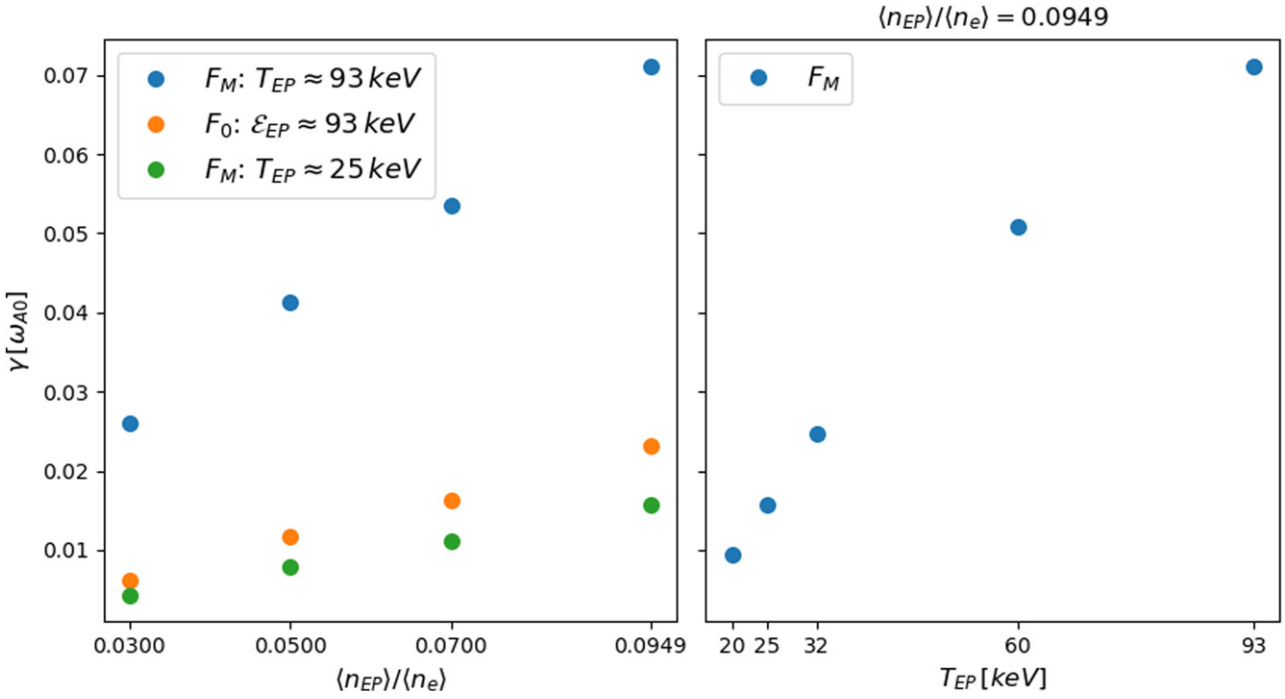

Figure 7. Growth rates determined in drift-kinetic simulations (no FLR effects). Left: scan against the EP concentration for Maxwellian (F_{M}) with constant temperature radial profile and slowing-down (F_0) distribution functions. $T_{\mathrm{EP}} = 25$ keV represents the value on the centre of the equivalent temperature (cf equation (27)) corresponding to an injection energy of $\mathcal{E}_{\mathrm{EP}} = 93$ keV. Right: scan against the EP temperature (constant against the radial position) in simulations where the EPs have been modelled through Maxwellian distribution functions.

a NB launched with an injection angle of 7.13° with respect to the horizontal plane. This experimental case exhibits, as anticipated in section 1, plasma parameters previously unexplored in AUG. In fact, the NB-induced fast-ion β is comparable to that of the bulk plasma and EPs' injection energy is approximately 100 times higher than the bulk species temperatures:

$$\beta_{\mathrm{EP}}/\beta_{\mathrm{Bulk}} \sim 1, \quad \mathcal{E}_{\mathrm{EP}}/T_{\mathrm{Bulk}} \approx 93\ \mathrm{keV}/1\ \mathrm{keV} \sim 10^2. \quad (20)$$

By doing so, the realistic ratios of plasma parameters that are going to be met in future fusion machines have been achieved in this scenario (in ITER/DEMO: $\mathcal{E}_{\mathrm{EP}}/T_{\mathrm{Bulk}} \approx 3.5$ MeV/30 keV). In such a way an intense EP-driven activity is observed, with the stabilizing effects of the bulk plasma minimized. That is why this is a very interesting scenario to understand the EP-driven dynamics and to validate the codes against the experiments. In particular this case presents a rich nonlinear physics of interest. Looking, in fact, at the experimental spectrogram in figure 1 we observe the presence of a series of TAE–EPM bursts after which EGAMs appear chirping. This suggests the presence of nonlinear interaction between AMs and EGAMs. We describe more in detail the EP-driven activity after the time $t = 0.84$ s at which the plasma parameters, profiles and magnetic equilibrium have been selected. In the temporal domain $0.841\ \mathrm{s} \leqslant t < 0.842$ s, corresponding to the region 1 in figure 1, an intense AM activity is present. Here the most unstable mode is an AM having, according to the pick-up-coils measurements, toroidal mode number $n = 1$. In this temporal window the AM frequency modification is indicated by the TAE–EPM burst that covers the frequency range $80\ \mathrm{kHz} \leqslant \nu \leqslant 250$ kHz. At the end of the TAE–EPM burst, at $t = 0.842$ s, an EGAM ($n = 0$) appears at lower frequencies ($\nu \approx 50$ kHz). It is now the most unstable mode in the temporal domain $0.842\ \mathrm{s} \leqslant t \leqslant 0.847$ s, corresponding to the region 2 in figure 1, where it exhibits the typical chirping behaviour. In figure 2 the temperature profiles of the bulk plasma species (left) and the radial dependence of the electron density profile (right) are shown, while in figure 3 left the radial dependence of the EP density profile n_{EP} modelled by TRANSP [35] is shown. The EPs have an off-axis radial density profile with a reference concentration of $\langle n_{\mathrm{EP}}\rangle/\langle n_{\mathrm{e}}\rangle = 0.0949$, where $\langle\cdots\rangle$ indicates volume average. In figure 3 right the radial dependence of the safety factor profile q is shown. It has a reversed shear, with a minimum around $r \approx 0.5$. Additionally the TAE position $r \approx 0.738$ is indicated (black point). This has been calculated through the analytical estimate [36] $r_0 : q_0 = q(r_0) = (2m_0 + 1)/(2n)$. This labels the radial position where two branches of the SAWs continuum calculated in cylindrical geometry having close poloidal harmonics m_0 and $m_0 + 1$, cross. Taking into account the realistic geometry (toroidal) of the system, the crossing of the SAW branches is removed and a gap is created by the interaction, in the case under investigation, between the two most unstable scalar potential Fourier components: $(m, n) = (2, 1)$ and $(m, n) = (3, 1)$. In table 1 the values of some important constants that will be used in the simulations are shown. In this work frequencies and growth rates will be provided in ω_{A0}-units, that is the Alfvén frequency on-axis, at $r = 0$: $\omega_{\mathrm{A0}} = v_{\mathrm{A}}(r = 0)/R_0$, with v_{A} the Alfvén speed (cf equation (2)) and R_0 the major radius of the tokamak.

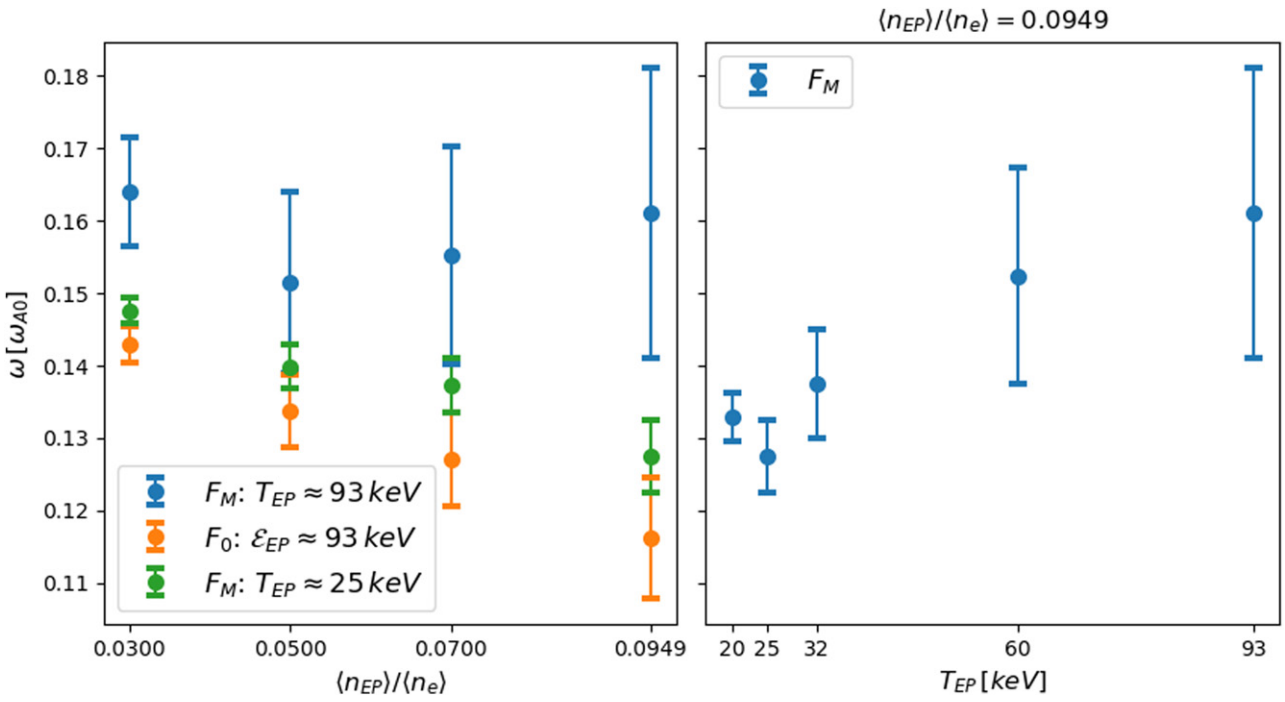

Figure 8. Real frequencies determined in the growing exponential phase of the dominant modes in drift-kinetic simulations (no FLR effects considered). Left: scan against the EP concentration for Maxwellian ($F_{\rm M}$) with constant temperature radial profile and slowing-down (F_0) distributions. Right: scan against the EP temperature (constant against the radial position) in simulations where the EPs have Maxwellian distribution functions.

Table 3. Growth rates γ and frequencies ω of the dominant modes, determined in drift-kinetic simulations (no FLR effects included). The reference EP concentration of $\langle n_{\rm EP}\rangle/\langle n_{\rm e}\rangle = 0.0949$ is here considered and the Maxwellian has a constant temperature radial profile.

Distribution function	$\gamma\ [\omega_{\rm A0}]$	$\omega\ [\omega_{\rm A0}]$
Slowing-down, $\mathcal{E}_{\rm EP} = 93$ keV	0.023	0.116 ± 0.008
Maxwellian, $T_{\rm EP} = 25$ keV	0.016	0.128 ± 0.005

Many works have already been dedicated to the investigation of the mode dynamics of this interesting experimental case. The linear AM dynamics has been investigated in references [28, 33] in simulations where both on-axis and off-axis radial density profiles have been considered for the EPs. These have been modelled via Maxwellian distribution functions associated to temperature profiles constant against the radius. In reference [37] numerical studies of the nonlinear EGAM dynamics have been conducted. In reference [38] bicoherence studies have suggested that nonlinear coupling exists between the observed TAE–EPM burst triggering the EGAM. In reference [29] the interaction between AMs and EGAMs has been studied both with numerical simulations and through an analytical model where only the EPs have been allowed to redistribute in phase-space, following their full trajectories. Additionally, there the EPs have been modelled via a double-bump-on-tail distribution function, since an anisotropy in velocity space was needed to drive an EGAM unstable [39–41].

In the present work we focus on the AM dynamics, modelling the bulk plasma species with Maxwellian distribution functions and retaining the nonlinearities only in the EP dynamics, as in [29, 33]. That is, only the EPs gyrocenter characteristics equations (7) to (9) have $\epsilon_\delta = 1$. The other particle species (electrons and bulk ions) follow their unperturbed trajectories and for them $\epsilon_\delta = 0$. The novelty of this work is represented by the fact that we go closer to the experimental conditions modelling the EPs via an isotropic slowing-down distribution function. We emphasize here that EPs are present in the NLED-AUG case as injected through an NB. This implies that their distribution function is intrinsically anisotropic in phase-space. In the studies carried out in this paper we neglect the effects of the anisotropy in velocity space that are, on the other hand, important to detail the interaction between AMs and EGAMs (that here we do not study in contrast to what was done in reference [29]). Nevertheless the isotropic slowing-down represents an improvement with respect to the Maxwellian distribution function, as will be motivated in section 4. Additionally through its choice we will observe a good quantitative comparison with the experiment making a further step with respect to previously published works where already a good qualitative agreement has been obtained. In the NLED-AUG scenario the bulk ions and the EPs are constituted by deuterium ions. In all the simulations discussed in this work the realistic electron mass will be considered: $m_{\rm e} \approx m_{\rm D}/3676$.

In section 4 we report a simplified analytical derivation and discuss why the slowing-down distribution function represents a better description of the EPs displacement in phase-space and

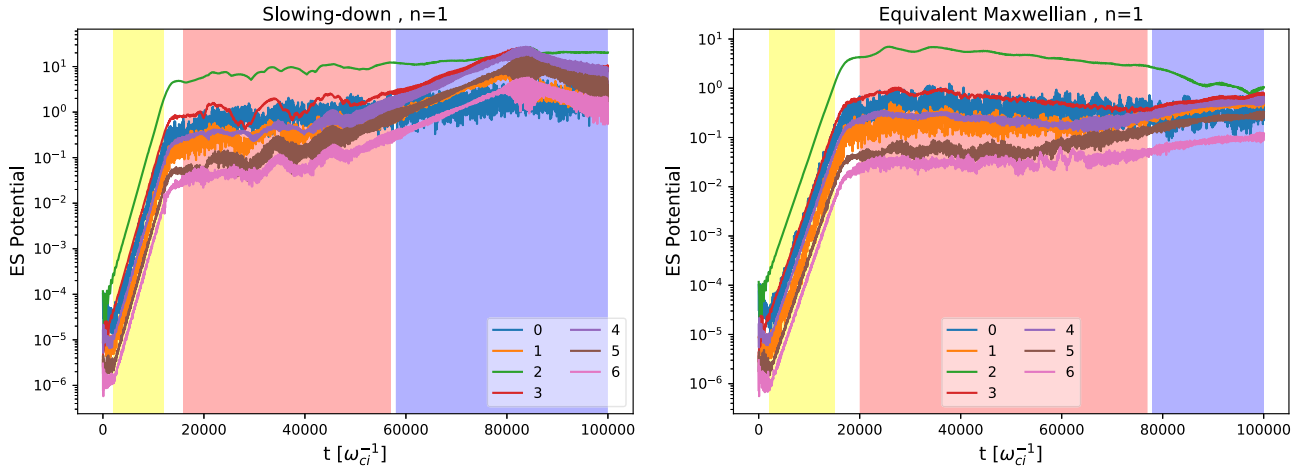

Figure 9. Temporal evolution of peak values for the dominant poloidal harmonics (m-numbers indicated in the legends) in the simulations. The initialized perturbation in the presented simulations has a Gaussian form, with dominant $m = 2, 3$. Left: EPs modelled with slowing-down distribution and $\mathcal{E}_{\rm EP} = 93$ keV. Right: EPs modelled with the equivalent Maxwellian.

Table 4. Growth rates γ and frequencies ω of the dominant modes, determined in gyrokinetic simulations (FLR effects of the EPs are retained). The reference EP concentration of $\langle n_{\rm EP}\rangle/\langle n_{\rm e}\rangle = 0.0949$ is here considered.

Distribution function	γ [$\omega_{\rm A0}$]	ω [$\omega_{\rm A0}$]
Slowing-down, $\mathcal{E}_{\rm EP} = 93$ keV	0.019	0.133 ± 0.007
Equivalent Maxwellian	0.015	0.138 ± 0.005

why this is an improvement with respect to the Maxwellian and the double-bump-on-tail distribution functions. Later we will describe its implementation in ORB5.

In all the simulations presented in section 5 the quasi-neutrality condition will always be satisfied $n_{\rm e} = Z_{\rm D} n_{\rm D} + Z_{\rm EP} n_{\rm EP}$ with $Z_{\rm D} = Z_{\rm EP} = 1$, by keeping fixed the electron radial density profile (cf figure 2 right) and varying accordingly the EP and bulk deuterium profiles.

4. Slowing-down distribution function

We want to investigate the AM dynamics in the NLED-AUG case with ORB5. Approximations are present in the performed simulations. The main approximations here concern the choice of not retaining the bulk plasma nonlinearities and the choice for the equilibrium distribution function of the particle species. The importance of modelling the particle species with a proper equilibrium distribution function can be understood by looking at the gyrokinetic Vlasov equation equation (6). In fact $\delta f_{\rm sp}$ can only be evolved once the equilibrium distribution function and its derivatives are known. Obviously changing the equilibrium distribution function implies a modification of the time evolution of the perturbed distribution function, thus catching different aspects of physics. While particles of the bulk plasma are usually well described by Maxwellian distribution functions (that from now on we denote with $F_{\rm M}$), the question here is what is the shape of the distribution function that better represents the arrangements of the EPs in phase-space. references [42–45] present a comprehensive theory describing the dynamic evolution of the EP equilibrium distribution functions, named 'phase space zonal structures', their governing equations as well as the corresponding phase space transport analysis. In this work, we choose a non-Maxwellian equilibrium distribution, namely the 'isotropic slowing-down' [30, 46–49]:

$$F_0 = \frac{n_{\rm EP}}{\frac{4\pi}{3}\log\left[1+\left(\frac{v_{\rm EP}}{v_{\rm c}}\right)^3\right]} \frac{\theta(v_{\rm EP}-v)}{v_{\rm c}^3+v^3} \quad \text{with} \quad v = |\boldsymbol{v}|,$$
$$v_{\rm EP} = \sqrt{2\mathcal{E}_{\rm EP}/m_{\rm EP}}. \tag{21}$$

In equation (21) $\mathcal{E}_{\rm EP}$ and $v_{\rm EP}$ are, respectively, the injection energy and velocity of EPs with mass $m_{\rm EP}$. $v_{\rm c}$ is the 'crossover velocity' or 'slowing-down critical velocity' defined as:

$$v_{\rm c} = \left(\frac{3\sqrt{\pi}}{4}\frac{m_{\rm e}}{m_{\rm EP}}Z_{\rm l}\right)^{1/3} v_{\rm th,\,e},$$
$$Z_{\rm l} = \sum_{i=\text{Bulkionsspecies}} \frac{n_{\rm i}}{n_{\rm e}}\frac{m_{\rm EP}}{m_{\rm i}}Z_i^2, \tag{22}$$

being Z_i the atomic number of the ith bulk ions species and $v_{\rm th,e}$ the electron thermal velocity. This isotropic slowing-down distribution function is appropriate to describe fusion-born products [48] since α particles are not born in any preferential direction (they are isotropic). On the other hand equation (21) does not appropriately describe the arrangement in phase-space of the EPs belonging to an injected ion beam. In this case, in fact, the EPs are not isotropic. Equation (21) represents nevertheless an improvement with respect to the Maxwellian distribution function and it is widely used in literature to model EPs [48]. In fact, through the Heaviside step function $\theta(v_{\rm EP} - v)$, it provides a constraint

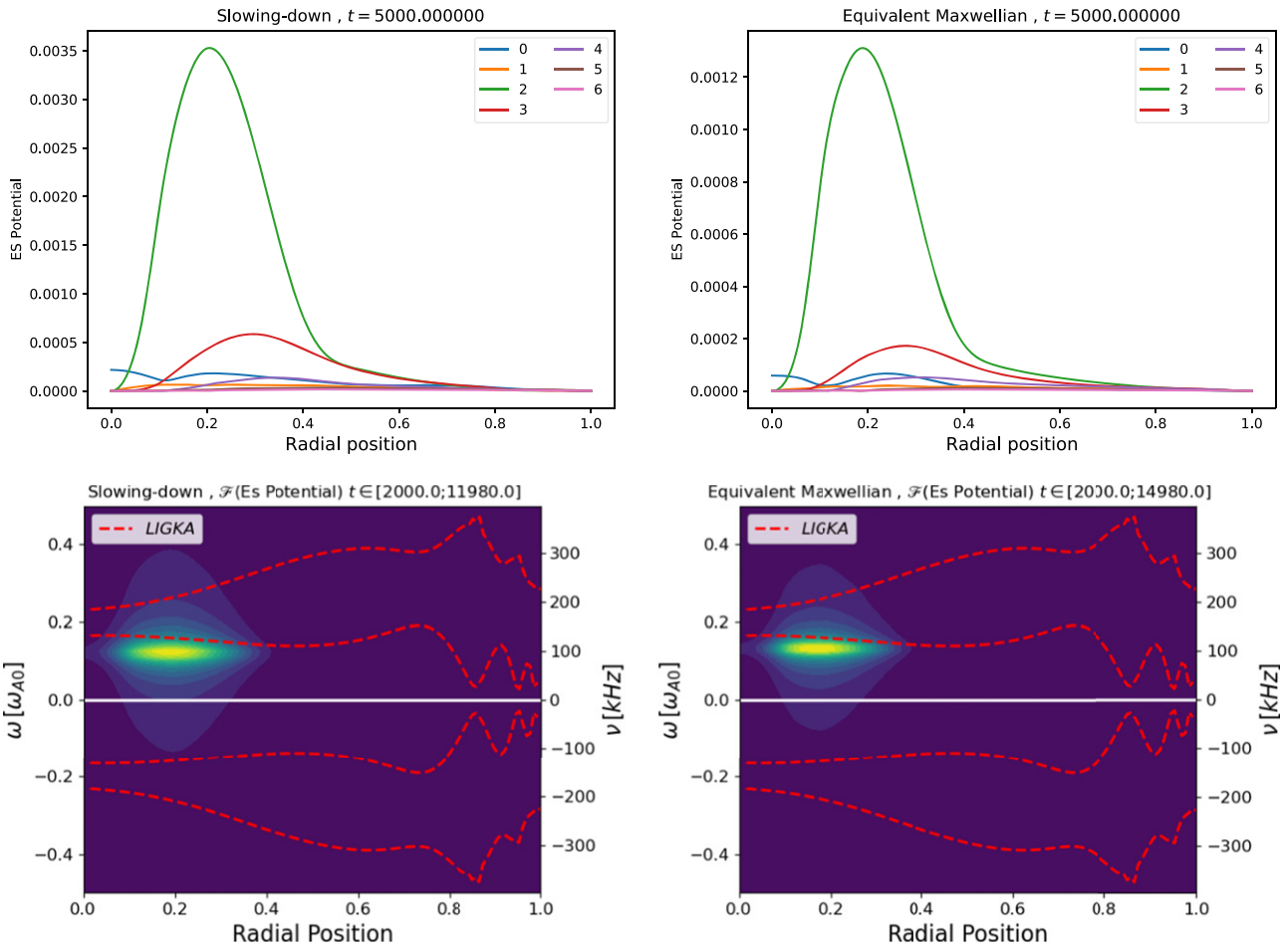

Figure 10. Mode structures and frequency spectra observed in the exponential growth phases (yellow regions) of the simulations in figure 9, where the EPs have been modelled with slowing-down (left) and equivalent Maxwellian (right).

in the velocity distribution of the EPs present (born/injected) in plasma with $\mathcal{E}_{\mathrm{EP}}$, since $0 \leqslant v \leqslant v_{\mathrm{EP}}$. Additionally its dependence in velocity-space is governed by the crossover velocity v_{c} that is a property of the bulk plasma and represents a threshold to determine the velocity regimes where EPs are mainly decelerated by frictions with bulk ions or electrons.

Equation (21) has been implemented in ORB5 together with its derivatives that are needed to evolve the perturbed EP distribution functions δf_{EP} equation (6):

$$\begin{cases} \dfrac{\mathrm{d}F_0}{\mathrm{d}\psi} = \left\{ \dfrac{\mathrm{d}}{\mathrm{d}\psi}\log n_{\mathrm{EP}} + \left(\dfrac{(v_{\mathrm{EP}}/v_{\mathrm{c}})^3}{\left[1+\left(\frac{v_{\mathrm{EP}}}{v_{\mathrm{c}}}\right)^3\right]\log\left[1+\left(\frac{v_{\mathrm{EP}}}{v_{\mathrm{c}}}\right)^3\right]} - \dfrac{v_{\mathrm{c}}^3}{v_{\mathrm{c}}^3+v^3} \right) \cdot 3\,\dfrac{\mathrm{d}}{\mathrm{d}\psi}\log v_{\mathrm{c}} \right\} F_0 \\ \dfrac{\mathrm{d}}{\mathrm{d}(m_{\mathrm{EP}}\mathcal{E})}F_0 = -\dfrac{3v}{v_{\mathrm{c}}^3+v^3}\dfrac{F_0}{m_{\mathrm{EP}}} \\ \dfrac{\mathrm{d}}{\mathrm{d}v_{\parallel}}F_0 = 0 \end{cases} \tag{23}$$

where $v = \sqrt{2\mathcal{E}}$ and:

$$\frac{\mathrm{d}v_{\mathrm{c}}}{\mathrm{d}\psi} = v_{\mathrm{c}}\left[\frac{\mathrm{d}}{\mathrm{d}\psi}\log v_{\mathrm{th,e}} - \frac{1}{3}\frac{\mathrm{d}}{\mathrm{d}\psi}\log n_{\mathrm{e}} + \frac{1}{3}\left(\sum_l \frac{z_l^2}{m_l}\frac{\mathrm{d}n_l}{\mathrm{d}\psi}\right)\cdot\left(\sum_p \frac{z_p^2}{m_p n_p}\right)\right], \tag{24}$$

where ψ is the normalized poloidal flux. In the notation in use:

$$\mathcal{E} = \frac{v^2}{2} = \frac{v_\parallel^2}{2} + \mu B \quad \text{with} \quad \mu = \frac{v_\perp^2}{2B} \quad \text{and} \quad \mathcal{E}_{\rm EP} = m_{\rm EP}\,\mathcal{E}. \tag{25}$$

We conclude this section introducing the concept of 'equivalent temperature' $T_{\rm EP}$ that is the temperature of a Maxwellian distribution function $F_{\rm M}$ for the EPs that satisfies the following requirement:

$$\int \mathrm{d}^3\vec{v}\, v^2\, F_{\rm M} = \int \mathrm{d}^3\vec{v}\, v^2\, F_0 \quad \text{with}$$

$$\int \mathrm{d}^3\vec{v}\, v^2\, F_{\rm M} = 3\, n_{\rm EP}(r)\frac{T_{\rm EP}(r)}{m_{\rm EP}} \tag{26}$$

from which it follows:

$$T_{\rm EP}(r) = \frac{2}{3}\frac{I_4\left(\frac{v_{\rm c}(r)}{v_{\rm EP}}\right)}{I_2\left(\frac{v_{\rm c}(r)}{v_{\rm EP}}\right)}\mathcal{E}_{\rm EP}, \tag{27}$$

where:

$$I_n(a) = \int_0^1 \mathrm{d}x \frac{x^n}{x^3 + a^3} = \begin{cases} n = 2, & \frac{1}{3}\ln(1 + a^{-3}) \\ n = 4, & \frac{1}{2} - a^2\left\{\frac{1}{6}\ln\left(\frac{1 - a + a^2}{(1+a)^2}\right) + \frac{1}{\sqrt{3}}\left[\tan^{-1}\left(\frac{2-a}{a\sqrt{3}}\right) + \frac{\pi}{6}\right]\right\}. \end{cases} \tag{28}$$

4.1. Implementation in ORB5

As it has been already anticipated in section 2, in ORB5 all the quantities are normalized with respect to reference parameters. In particular, velocities are given in units of the sound velocity $c_{\rm s}$:

$$c_{\rm s} = \sqrt{\frac{T_{\rm e}(r_0)}{m_{\rm D}}} \tag{29}$$

defined as the square root of the electron temperature considered at a chosen reference position r_0, divided by the mass of the main ion species that, for the NLED-AUG case, is constituted by deuterium ions. Here the reference radial position is on-axis $r_0 = 0$ and $T_{\rm e}(r_0) = 0.7088$ keV. In figure 4 the velocity dependence in $(v_\parallel, \mu B)$-space of the slowing-down distribution function at $r = 0.5$ is shown. This has been taken from an ORB5-simulation. It has been obtained considering the bulk plasma parameters of the NLED-AUG case (see section 3) as well as the reference EPs parameters: off-axis radial density profile in figure 3 left having a concentration of $\langle n_{\rm EP}\rangle/\langle n_{\rm e}\rangle = 0.0949$, injected with injection energy $\mathcal{E}_{\rm EP} = 93$ keV. In figure 5 slices obtained from figure 4 are shown. There we can observe the cuts in velocity-space introduced because of the presence of the Heaviside function in equation (21):

$$v_\parallel \approx 16.2\, c_{\rm s}, \quad \mu B \approx 131.1\, c_{\rm s}^2\,. \tag{30}$$

Using the appropriate conversion factor the interested reader can easily verify that these cuts correspond to an injection energy of $\mathcal{E}_{\rm EP} = 93$ keV. In figure 6 we show the EP radial density profile (on the top) and the equivalent temperature (on the bottom). There, the analytical expressions indicated by the black dashed lines correspond on the top to figure 3 left and on the bottom to equation (27). These are compared with the corresponding moments of F_0 (blue lines) calculated through numerical integration in velocity space of the distribution function implemented in ORB5. The observed good agreement between the analytical expressions and the numerical calculations is a further proof of the correct implementation of the new non-Maxwellian background distribution function in the code.

5. Comparison with the experiments: application to the NLED-AUG case

We discuss here the mode dynamics observed in numerical simulations where the NLED-AUG scenario (see section 3) has been taken into account. In table 2 the main parameters considered in the simulations are reported. Their choice is motivated by convergence studies (see appendix A). As it is indicated in table 2, we will investigate here only the dynamics of modes with toroidal mode number $n = 1$. This because, as anticipated in section 3, from experimental measurements this is known to be the most unstable AM. The dynamics of zonal structures ($n = 0$) is then not treated in the present work. We begin studying the mode dynamics observed in the exponential growth phase of the dominant mode. We compare the results obtained with a Maxwellian distribution with constant temperature radial profile ($F_{\rm M}$), with those obtained with an isotropic slowing-down (F_0). For the moment, we run ORB5 neglecting the FLR effects of all the particle species, i.e. considering a drift-kinetic model. In all the simulations analysed the dominant mode, in the exponential growth phase, is an AM with scalar potential dominated by its components $(m, n) = (2, 1)$ and peaked around $r = 0.2$. In figure 7 left the growth rates determined in a scan against the EP concentration are shown. There the EPs have been modelled, as indicated in the legend, with isotropic slowing-down (orange points) and with Maxwellians with constant temperature radial profiles of, respectively, $T_{\rm EP} = 93$ keV (blue points) and $T_{\rm EP} = 25$ keV (green points). Note that this last corresponds to the value of the equivalent temperature around $r \approx 0.5$ for an isotropic slowing-down with injection energy of $\mathcal{E}_{\rm EP} = 93$ keV, as discussed in section 4.1 and indicated in figure 6 bottom. In figure 7 right the growth rate dependence against the EP temperature (with constant radial profile)

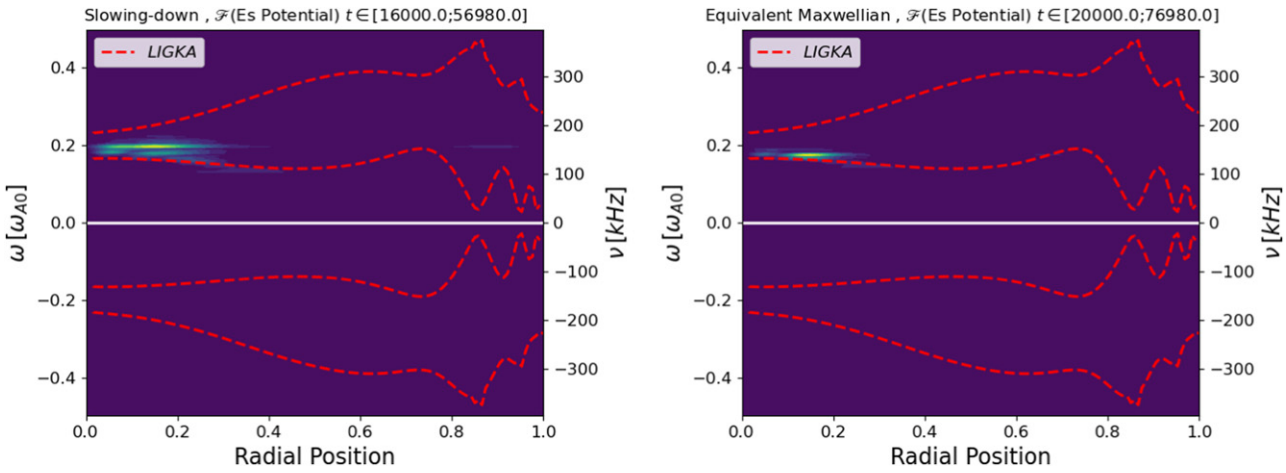

Figure 11. Frequency spectra calculated in the early nonlinear phases (pink regions) of the simulations in figure 9. Left: EPs modelled with slowing-down distribution function. Right: EPs modelled via equivalent Maxwellian.

is shown in a scan where the EPs have been modelled via Maxwellian distribution functions and the reference EP concentration of $\langle n_{EP}\rangle/\langle n_e\rangle = 0.0949$ has been taken into account. In figure 8 we display the real frequencies of the dominant modes observed in the corresponding simulations that have produced the growth rates reported in figure 7. Only in figure 8 the error bars are present, since the errors committed determining the growth rates in figure 7 are negligible. In figure 8 the presented error bars correspond to the full width at half maximum of the peaks in the frequency spectrum. In the scans presented in figures 7 and 8, the case closer to the experimental conditions is that where the EPs have been modelled with slowing-down distribution function and concentration of $\langle n_{EP}\rangle/\langle n_e\rangle = 0.0949$. Its values of growth rate and frequency are reported in table 3. There, they are compared with those obtained in a simulation with same EP concentration but with Maxwellian distribution function with constant temperature radial profile of $T_{EP} = 25$ keV. Referring to table 3, we can then conclude that the choice of the slowing-down distribution function over a Maxwellian distribution function with temperature close to the equivalent temperature, does not affect significantly the frequency of driven AM, although quantitative differences as large as almost 40% are found in the growth rate. The same trend is found comparing, in figure 7 left and figure 8 left, the set of orange points with the green points. By modelling the EPs with different distribution functions, the contribution of the velocity gradients to the total growth rate of the driven mode is modified [50] and this is held responsible of the differences observed in the total growth rates. In future works, further and more accurate investigations will be carried out by extending the electrostatic power-balance diagnostics already present in ORB5 [51] to the electromagnetic version. We describe now in detail the mode dynamics of the AM observed in simulations where FLR effects are included for bulk ions and EPs (the model is gyrokinetic) and the reference EP concentration of $\langle n_{EP}\rangle/\langle n_e\rangle = 0.0949$ is taken into account. Here we will not just limit ourselves to the investigation of the exponential growth phase of the AM, but also to its nonlinear phase. There the AM mode structure evolves

Table 5. Growth rates γ of $(m, n) = (3, 1)$ in the deep nonlinear phase (blue regions in figure 9). Gyrokinetic simulations (FLR effects of the EPs are retained). The reference EP concentration of $\langle n_{EP}\rangle/\langle n_e\rangle = 0.0949$ is here considered.

Distribution function	$\gamma\ [\omega_{A0}]$
Slowing-down, $\mathcal{E}_{EP} = 93$ keV	0.002
Equivalent Maxwellian	0.000 53

radially, presenting peaks close to the edge. Therefore we have increased the radial resolution to $N_r = 6000$ in order to correctly resolve those peaks. Simultaneously since in ORB5 the numerical noise is proportional to the number of radial grid points N_r [52], we have increased the number of markers to $nptot_{D,e,EP} = (18, 72, 18) \cdot 10^7$.

The temporal dynamics observed in a simulation where the EPs have been modelled with the slowing-down distribution function with $\mathcal{E}_{EP} = 93$ keV, is compared with that observed in a simulation where the EPs are modelled with the equivalent Maxwellian (the equivalent temperature in figure 6 is taken now into account). The former is shown in figure 9 left, while the latter is shown in figure 9 right. In the two plots in figure 9 we have highlighted the temporal intervals corresponding to: the exponential growth phase (yellow), the early nonlinear phase (pink) and the deep nonlinear phase (blue). Note that both the simulations cover the same temporal range: $t \in [0; 100\,000]\,\omega_{ci}^{-1}$.

The growth rate and frequencies determined in the exponential growth phase of the two simulations in figure 9 are reported in table 4, while the corresponding mode structures and frequency spectra are shown in figure 10. The dominant AM here, as in the drift-kinetic simulations, is an EPM whose scalar potential is dominated by the Fourier component $(m, n) = (2, 1)$ peaked around the radial position $r \approx 0.2$. Its frequency lies almost on the continuum spectrum calculated with the linear gyrokinetic code LIGKA [53] (see red dashed lines in figure 10 on the bottom). We can conclude also here that, as for the drift-kinetic simulations, the choice of the equivalent Maxwellian over the slowing-down

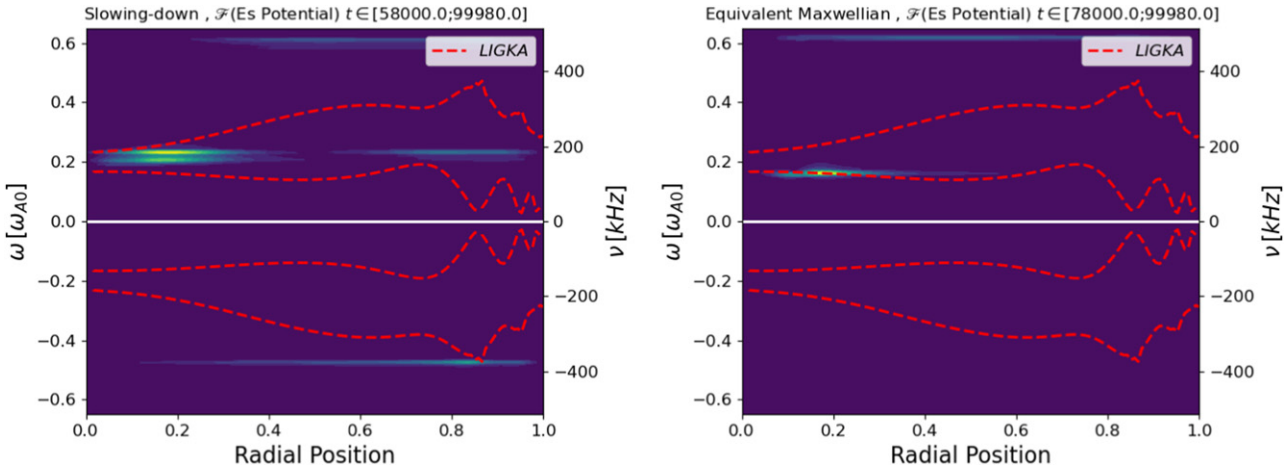

Figure 12. Frequency spectra calculated in the deep nonlinear phases (blue regions) of the simulations in figure 9. Left: EPs modelled with slowing-down distribution function. Right: EPs modelled via equivalent Maxwellian.

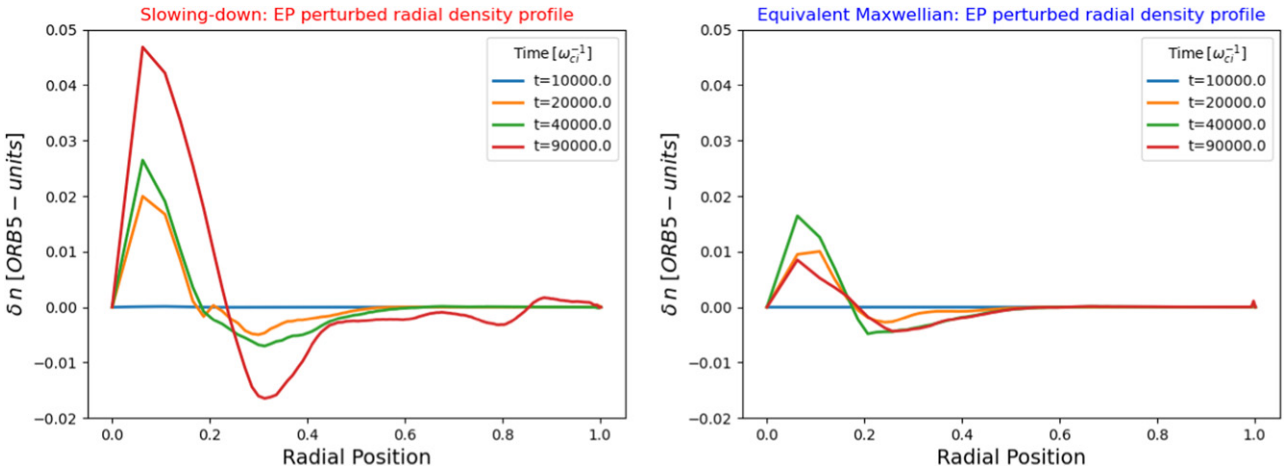

Figure 13. EP perturbed radial density profile $\delta n = \langle \delta f_{\mathrm{EP}} \rangle_v$. δf_{EP} is the perturbed EP distribution function and $\langle \cdots \rangle_v$ indicates integration in velocity space.

distribution function, does not modify significantly the kind of driven AM investigated (mode structure and frequency). However, referring to table 4, we still observe a growth rate quantitative difference that in this case is as large as almost 30% of the value of the growth rate obtained in the simulation with the EPs modelled with the equivalent Maxwellian.

In figure 11 we compare the frequency spectra calculated in the early nonlinear phases (pink regions) of the two different simulations shown in figure 9. In this temporal phase the scalar potential Fourier component $(m, n) = (2, 1)$ is still the dominant one, since it is almost an order of magnitude higher than the other Fourier components. Comparing figure 11 with figure 10, we observe that both simulations catch correctly the nonlinear modification of the AM frequency passing from the linear to the nonlinear phase. In this time interval, the dominant AM frequency exhibits tiny differences modelling the EPs with slowing-down or equivalent Maxwellian. Additionally in both simulations, at the end of this phase, the Fourier component $(m, n) = (3, 1)$ begins to grow, even though with different growth rate, as indicated in table 5.

In figure 12 the frequency spectra calculated in the deep nonlinear phases (blue regions in figure 9) are shown. In these temporal phases the scalar potential Fourier component $(m, n) = (3, 1)$ reaches an amplitude comparable to that of the dominant $(m, n) = (2, 1)$. Passing from figures 11 to 12 we observe that in the simulation where the EPs have been modelled with the slowing-down (left), a higher frequency modification of the AM is detected with respect to the right plots where the EPs had been modelled with the equivalent Maxwellian. By comparing, in fact, figure 11 left with figure 12 left it becomes clear that the EPM chirps up reaching the TAE gap. On the contrary this behaviour is not observed modelling the EPs with the equivalent Maxwellian (cf figure 11 right with figure 12 right). In the former case a global mode structure is formed. This is located not only in the central radial region where the EPM was originally observed, but also in the outer radial domain. The AM arising in this nonlinear phase oscillates then mainly at the TAE frequency.

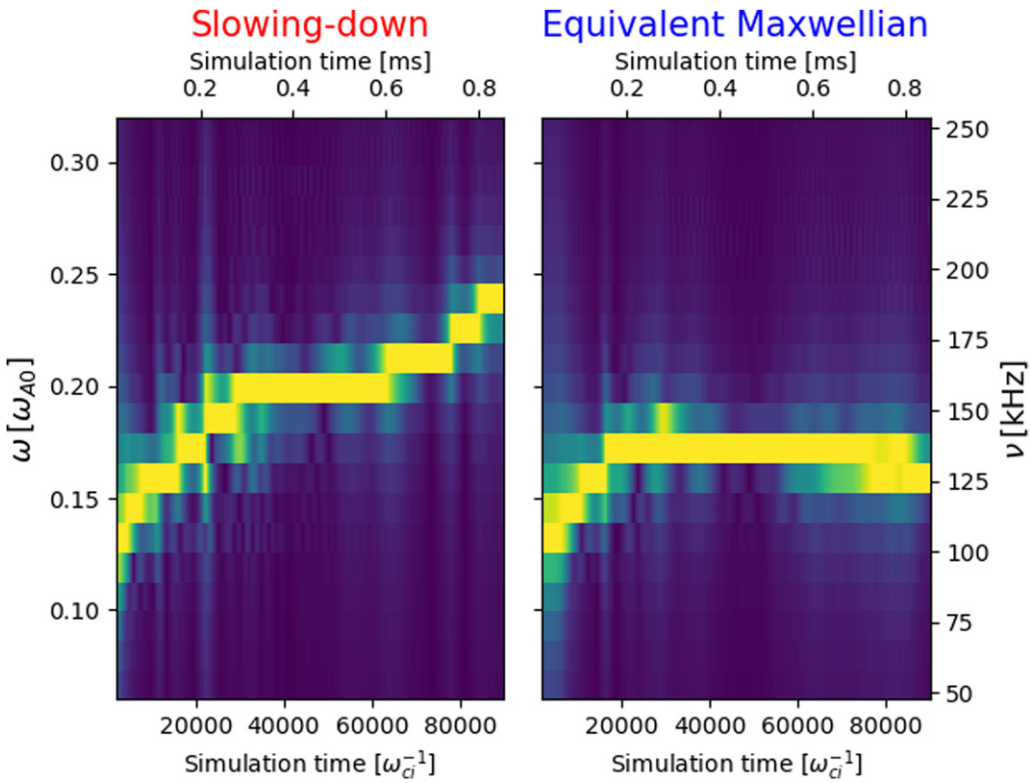

Figure 14. Spectrograms calculated from ORB5 simulations with the EPs modelled with different distribution functions (as indicated in the plot titles). The Fourier transform of the signal has been calculated in the temporal range $t \in [t_0, t_0 + \Delta t]$ with $\Delta t = 10^4\,\omega_{\rm ci}^{-1}$. The low boundary t_0 has been varied continuously as indicated in the x-axis of the plot.

We remind here that this is an AE whose frequency lies inside the gap created by the branches of the continuum (m_0, n) and $(m_0 + 1, n)$ at the radial position r_0 that labels the rational surface satisfying $q(r_0) = (2m_0 + 1)/(2n)$ [13] where two close poloidal harmonics interact. For the case under investigation: $m_0 = 2$, $n = 1$ and $r_0 = 0.738$ (cf figure 3 right). The formation of the extended mode structure in figure 12 left has a consequence also in the EP transport, as it can be appreciated in figure 13. There the radial structure of the perturbed EP density profile δn is shown at different times for the simulation with the EPs modelled with isotropic slowing-down (left plot) and equivalent Maxwellian (right plot). We observe, indeed, that in the second half of the radial domain of figure 13 left the EPs are redistributed outward as it is expected by the TAE presence. Additionally by coupling to the TAE gap the AM results less affected by continuum damping. This reduction in damping leads to a further growth of the mode in the nonlinear phase of figure 9 left with respect to figure 9 right. This is held responsible of the difference in the final saturation levels observed in the two mentioned simulations. We emphasize that while in figure 12 left the AM oscillates almost at every radial position at the TAE frequency, in figure 12 right, such a higher frequency modification is not observed. The nonlinear frequency modification from the EPM to the TAE observed modelling the EPs with isotropic slowing-down results then more in agreement with the experiment with respect to the frequency modification observed modelling the EPs with equivalent Maxwellian. Finally we note in figure 12 the presence, in this deep nonlinear phase, of higher frequencies in the EAE gap: $\omega \sim 0.6, -0.5\omega_{\rm A0}$. We do not further investigate the emerging of these higher frequencies as the focus of the present paper is on the study of the TAE–EPM frequency modification observed in the experiment (cf figure 1), that correspond to the dominant frequencies also in the presented simulations.

We summarize the presented results of the AM frequency modification in figure 14. There the numerical spectrogram calculated in a simulation with EPs modelled with the slowing down (left) is compared with that obtained in the simulation where the EPs have been modelled with the equivalent Maxwellian (right). The spectrograms presented have been obtained through the fast Fourier transform of the scalar potential at $r = 0.2$. This corresponds to the radial positions where the mode structure of the AM has a maximum. The time interval where the Fourier transform has been calculated $[t_0;\ t_0 + \Delta t]$ has been obtained varying continuously t_0 (as indicated in the x-axis in figure 14) and choosing $\Delta t = 10^4\,\omega_{\rm ci}^{-1}$. In figure 14 the time units are provided also in milliseconds, while the frequency units are provided also in kHz, to allow a better comparison with the experimental spectrogram in figure 1.

As it can be noticed in figure 14, by modelling the EPs with the isotropic slowing-down rather than with the equivalent Maxwellian, a broader AM frequency modification in the nonlinear phase is observed: 100 kHz $\leqslant \nu \leqslant$ 180 kHz. This

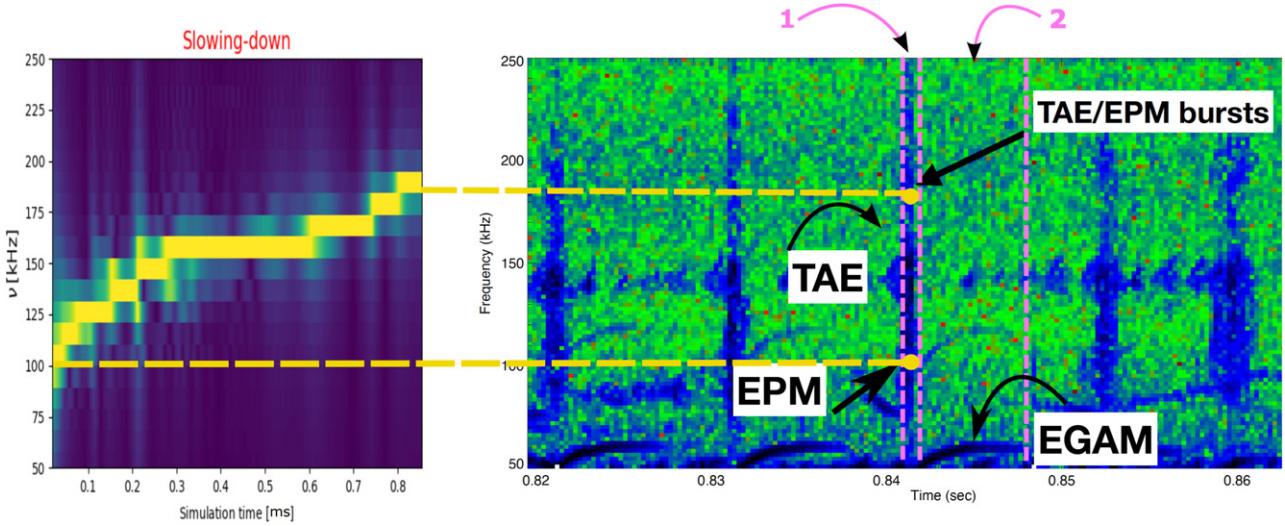

Figure 15. Experimental spectrogram (right, corresponding to figure 1) compared with the numerical spectrogram (left) obtained modelling the EPs with the isotropic slowing-down and corresponding to figure 14 on the left.

results in better agreement with the experiment, as it can be appreciated in figure 15. There, the experimental spectrogram (right plot, corresponding to figure 1) is shown again. It is compared with the left plot corresponding to the spectrogram already presented in figure 14 and obtained from a simulation with the EPs modelled with the isotropic slowing-down. In addition to the AM frequency modification, we observe that the total simulated time is approximately $\Delta t \approx 1$ ms (cf figure 15 left). This corresponds, approximately, to the temporal width of region number 1 in figure 15 right, contained between the first two vertical dashed purple lines starting from the left. Region number 1 corresponds to the time interval where the TAE–EPM burst is present while the EGAM is absent. The observed agreement between the experiment and the numerical simulations is already encouraging. However in the future, more accurate studies will be carried out to reproduce the full frequency modification of the TAE–EPM burst that, as anticipated in section 3, covers a broader frequency range than that reproduced in the simulations: 80 kHz $\leqslant \nu \leqslant$ 250 kHz.

6. Conclusion

In this work the study of the AM instabilities driven by EPs has been conducted for the NLED-AUG scenario. This is an interesting case obtained in the Tokamak AUG where the EPs have been injected through a NB with energy $\mathcal{E}_{\mathrm{EP}} \approx 93$ keV. The peculiarity of this scenario relies on the fact that it has been obtained through plasma ratios ($\beta_{\mathrm{EP}}/\beta_{\mathrm{Bulk}}$ and $\mathcal{E}_{\mathrm{EP}}/T_{\mathrm{Bulk}}$) close to those that are going to be met in future fusion machines.

Studies of the AM dynamics in the NLED-AUG case have already been conducted through numerical simulations [28, 29, 33]. The main novelty in the present work is represented by the fact that the EPs have been modelled thorough an equilibrium isotropic slowing-down distribution function. Through it, we have been able to go closer to the experimental conditions. We have obtained a good quantitative agreement with the experimental spectrogram doing a further step with respect to previous published works [28, 33] where the focus was on the driven AM and on its characterization. In the present work we have studied, for the first time, the AM frequency modification in the nonlinear phase. We have shown that the choice of the isotropic slowing-down over the equivalent Maxwellian allows a more accurate description of the AM frequency modification, resulting in a better agreement with the experiment. Interestingly we have also observed, in the former case, an increase in the saturation level of the AM that is imputed to the chirping up of the EPM that, by coupling to the TAE gap, results less affected by damping. Consequently a mode with extended mode structure is formed that enhances the outer EP redistribution. These results are already encouraging and prove that we are able to reproduce the relevant physics behind the experiments in an attempt to become predictive about future fusion scenarios and pave the path to new studies that have to be carried out to catch more of the nonlinear aspects in the NLED-AUG case. In future works we will carry out further studies to reproduce the full frequency modification of the AM observed in the experiment that in the current work is not entirely portrayed. Additionally we will retain the nonlinearities in all the particle species and we will consider the interaction between the AM and the EGAM, to describe the triggering of the EGAM by the TAE–EPM burst. An attempt on this has already been done in reference [29] where the EPs have been modelled with a double-bump-on-tail. Moreover the AM and EGAM interaction will be studied considering a ξ-dependent slowing-down distribution function [54] in order to retain the anisotropy in velocity space needed to drive the EGAM.

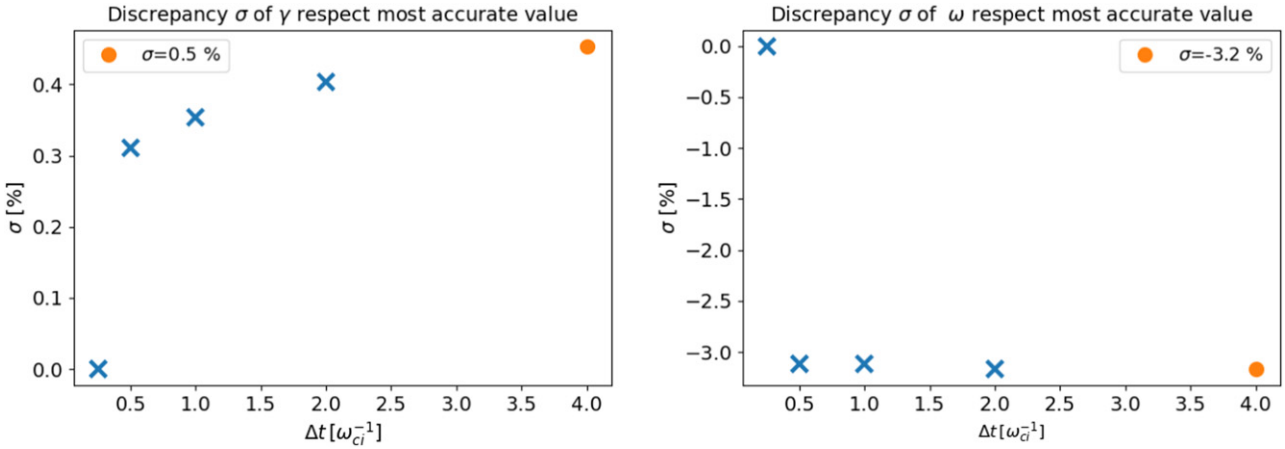

Figure 16. Simulations with # of markers$_{\mathrm{D,e,EP}} = (3, 12, 3) \cdot 10^7$ and $N_\mathrm{r} = 1000$. Scan against the time step Δt in use in the simulations. In the plots, the discrepancies σ of growth rate (left) and frequencies (right) with respect to the best resolved case (at $\Delta t = 0.25\,\omega_{\mathrm{ci}}^{-1}$) are shown. The orange points correspond to the results obtained with the parameters shown in table 6.

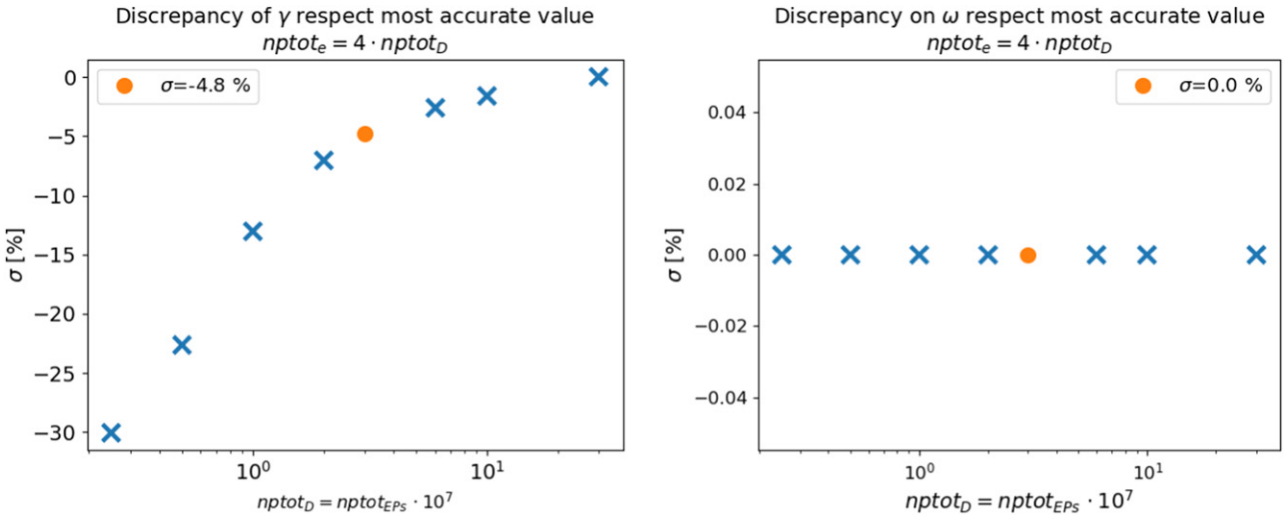

Figure 17. Simulations with $\Delta t = 4\,\omega_{\mathrm{ci}}^{-1}$ and $N_\mathrm{r} = 1000$. Scan against the # of markers of deuterium and EPs. The number of markers for the electrons is four times higher than that of the EPs. In the plots the discrepancies σ of growth rate (left) and frequencies (right) with respect to the best resolved case (corresponding to the simulation with number of markers $= 30 \cdot 10^7$) are shown. The orange points correspond to the results obtained with the parameters shown in table 6.

Acknowledgments

Simulations presented in this work were performed on the CINECA Marconi supercomputer within the ORBFAST, OrbZONE and TSVV10 projects. The authors acknowledge stimulating discussions with Z. Lu, F. Zonca, S. Briguglio, I. Novikau and A. Di Siena. This work was partly performed in the frame of the 'Multi-scale Energetic Particle Transport in Fusion Devices' ER project. This work has been carried out within the framework of the EUROfusion Consortium, funded by the European Union via the Euratom Research and Training Programme (Grant Agreement No. 101052200—EUROfusion). Views and opinions expressed are however those of the author(s) only and do not necessarily reflect those of the European Union or the European Commission. Neither the European Union nor the European Commission can be held responsible for them.

Appendix A. Slowing-down validation and convergence studies

We present here a series of convergence studies used to find the reference simulation parameters in table 2. In figures 16, 17, 18 and 19 we show the discrepancies σ of the determined quantities X from the most accurate value, that is:

$$\sigma\,[\%] = \frac{X - X_{\mathrm{mostaccuratevale}}}{X_{\mathrm{mostaccuratevale}}} \cdot 100. \tag{31}$$

The most accurate value $X_{\text{most accurate value}}$ corresponds to the value (almost) at convergence. Its discrepancy, because of the definition in equation (31), is $\sigma = 0\%$. In figures 16, 17, 18 and 19 the orange points have been obtained in simulations where the reference parameters in table 6 have been considered.

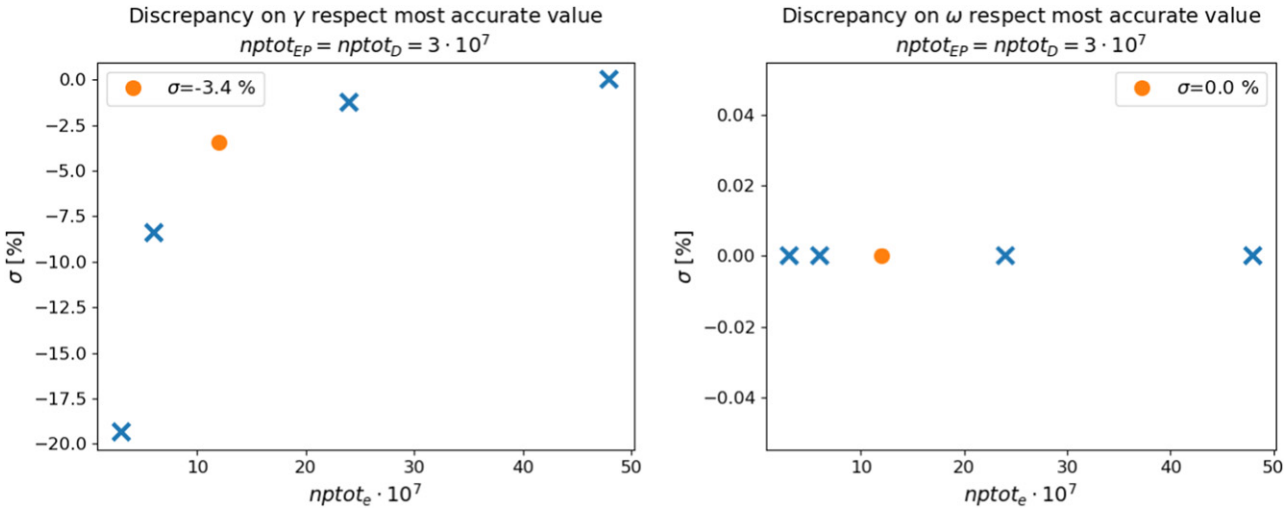

Figure 18. Simulations with $\Delta t = 4\,\omega_{ci}^{-1}$ and $N_r = 1000$. Scan against the # of markers of the electrons. The number of markers for EPs and deuterium particles is fixed at $3 \cdot 10^7$. In the plots the discrepancies σ of growth rate (left) and frequencies (right) with respect to the best resolved case (here corresponding to the simulation with number of markers $= 50 \cdot 10^7$) are shown. The orange points correspond to the results obtained with the parameters shown in table 6.

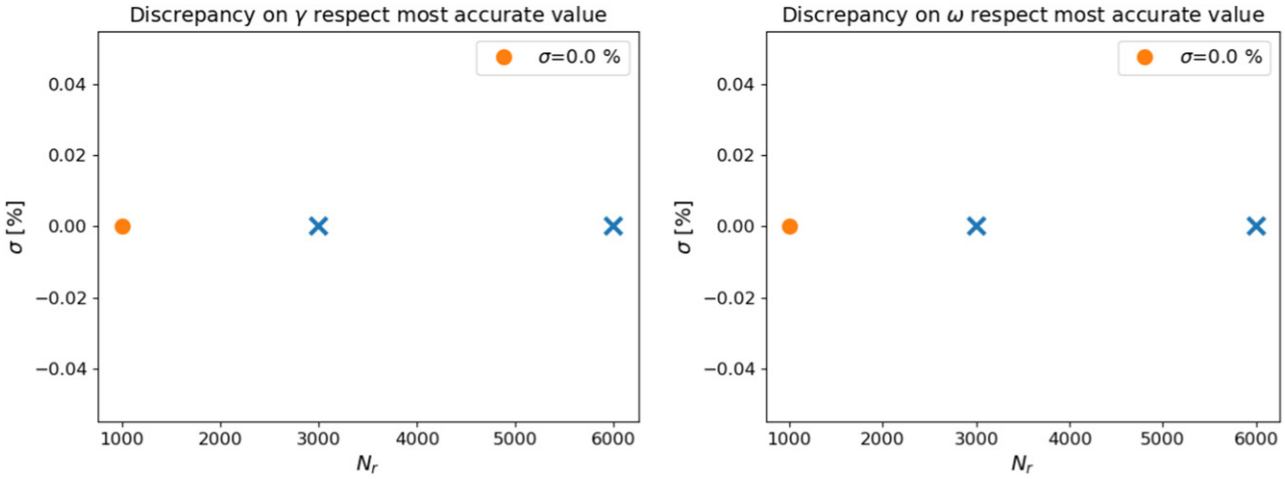

Figure 19. Simulations with $\Delta t = 4\,\omega_{ci}^{-1}$ and # of markers$_{D,e,EP} = (3, 12, 3) \cdot 10^7$. Scan against the # of radial grid points N_r. In the plots the discrepancies σ of growth rate (left) and frequencies (right) with respect to the best resolved case (here corresponding to the simulation with $N_r = 6000$) are shown. The orange points correspond to the results obtained with the parameters shown in table 6.

Table 6. Reference simulation parameters: time step (Δt), number of markers for particle species ($nptot$) and radial grid points (N_r), cf section 2.

$\Delta t\,[\omega_{ci}^{-1}]$	$nptot_{D,e,EP} \cdot 10^7$	N_r
4	3, 12, 3	1000

In all the simulations here presented FLR effects are retained and the reference EP concentration of $\langle n_{EP}\rangle/\langle n_e\rangle = 0.0949$ is considered. The quantities X here studied (growth rates γ and frequencies ω) have been determined in the exponential growth phase of the simulations. The scans here presented are against: the time width Δt, the number of markers $nptot$ and the number of radial grid points N_r (cf section 2). The growth rate and frequency obtained using the reference parameters in table 6 correspond to:

$$\gamma_{ref} = 0.0197\,\omega_{A0}, \quad \omega_{ref} = 0.133\,\omega_{A0}. \tag{32}$$

ORCID iDs

F. Vannini https://orcid.org/0000-0002-0103-0362
A. Biancalani https://orcid.org/0000-0002-7227-6343
A. Bottino https://orcid.org/0000-0002-0514-8851
T. Hayward-Schneider https://orcid.org/0000-0003-0588-5090
A. Mishchenko https://orcid.org/0000-0003-1436-4502
E. Poli https://orcid.org/0000-0001-7552-4800
B. Rettino https://orcid.org/0000-0002-1517-1932
G. Vlad https://orcid.org/0000-0003-1482-5436
X. Wang https://orcid.org/0000-0002-3756-1771

References

[1] Tomabechi K., Gilleland J.R., Sokolov Y.A. and Toschi R. 1991 ITER conceptual design *Nucl. Fusion* **31** 1135–224

[2] Zohm H. *et al* 2013 On the physics guidelines for a tokamak DEMO *Nucl. Fusion* **53** 073019

[3] Heidbrink W.W. and Sadler G.J. 1994 The behaviour of fast ions in tokamak experiments *Nucl. Fusion* **34** 535–615

[4] Mahajan S.M. 1995 Spectrum of Alfvén waves, a brief review *Phys. Scr.* **T60** 160–70

[5] Vlad G., Zonca F. and Briguglio S. 1999 Dynamics of Alfvén waves in tokamaks *Riv. Nuovo Cimento* **22** 1–97

[6] Barston E.M. 1964 Electrostatic oscillations in inhomogeneous cold plasmas *Ann. Phys., NY* **29** 282–303

[7] Sedláček Z. 1971 Electrostatic oscillations in cold inhomogeneous plasma: I. Differential equation approach *J. Plasma Phys.* **5** 239–63

[8] Grad H. 1969 *Phys. Today* **22** 34

[9] Lauber P. 2013 Super-thermal particles in hot plasmas-kinetic models, numerical solution strategies, and comparison to tokamak experiments *Phys. Rep.* **533** 33–68

[10] Heidbrink W.W. 2008 Basic physics of Alfvén instabilities driven by energetic particles in toroidally confined plasmas *Phys. Plasmas* **15** 055501

[11] Chen L. and Zonca F. 2016 Physics of Alfvén waves and energetic particles in burning plasmas *Rev. Mod. Phys.* **88** 015008

[12] Chen L. 1994 Theory of magnetohydrodynamic instabilities excited by energetic particles in tokamaks *Phys. Plasmas* **1** 1519–22

[13] Cheng C.Z., Chen L. and Chance M.S. 1985 High-*n* ideal and resistive shear Alfvén waves in tokamaks *Ann. Phys., NY* **161** 21–47

[14] Cheng C.Z. and Chance M.S. 1986 Low-*n* shear Alfvén spectra in axisymmetric toroidal plasmas *Phys. Fluids* **29** 3695–701

[15] Heidbrink W.W., Strait E.J., Doyle E., Sager G. and Snider R.T. 1991 An investigation of beam driven Alfvén instabilities in the DIII-D tokamak *Nucl. Fusion* **31** 1635–48

[16] Sharapov S.E. *et al* 2002 Alfvén wave cascades in a tokamak *Phys. Plasmas* **9** 2027–36

[17] Berk H.L., Borba D.N., Breizman B.N., Pinches S.D. and Sharapov S.E. 2001 Theoretical interpretation of Alfvén cascades in tokamaks with nonmonotonic q profiles *Phys. Rev. Lett.* **87** 185002

[18] McGuire K. *et al* 1983 Study of high-beta magnetohydrodynamic modes and fast-ion losses in PDX *Phys. Rev. Lett.* **50** 891–5

[19] White R.B., Goldston R.J., McGuire K., Boozer A.H., Monticello D.A. and Park W. 1983 Theory of mode-induced beam particle loss in tokamaks *Phys. Fluids* **26** 2958–65

[20] Sigmar D.J., Hsu C.T., White R. and Cheng C.Z. 1992 Alpha-particle losses from toroidicity-induced Alfvén eigenmodes: II. Monte Carlo simulations and anomalous alpha-loss processes *Phys. Fluids* B **4** 1506–16

[21] Shinohara K. *et al* 2001 Alfvén eigenmodes driven by Alfvénic beam ions in JT-60U *Nucl. Fusion* **41** 603–12

[22] Shinohara K. *et al* 2004 Energetic particle physics in JT-60U and JFT-2M *Plasma Phys. Control. Fusion* **46** S31–45

[23] Ishikawa M. *et al* (the JT-60 team) 2005 Energetic ion transport by abrupt large-amplitude event induced by negative-ion-based neutral beam injection in the JT-60U *Nucl. Fusion* **45** 1474–80

[24] Bierwage A., Shinohara K., Todo Y., Aiba N., Ishikawa M., Matsunaga G., Takechi M. and Yagi M. 2018 Simulation tackle abrupt massive migrations of energetic beam ions in tokamak plasma *Nat. Commun.* **9** 3282

[25] Lanti E. *et al* 2020 ORB5: a global electromagnetic gyrokinetic code using the PIC approach in toroidal geometry *Comput. Phys. Commun.* **251** 107072

[26] Lauber P. Studies and details on the NLED-AUG case (https://pwl.home.ipp.mpg.de/NLED_AUG//data.html)

[27] Qiu Z. and Chen L. 2011 Kinetic theories of geodesic acoustic modes: radial structure, linear excitation by energetic particles and nonlinear saturation *Plasma Sci. Technol.* **13** 257–66

[28] Vannini F., Biancalani A., Bottino A., Hayward-Schneider T., Lauber P., Mishchenko A., Novikau I. and Poli E. 2020 Gyrokinetic investigation of the damping channels of Alfvén modes in ASDEX Upgrade *Phys. Plasmas* **27** 042501

[29] Vannini F., Biancalani A., Bottino A., Hayward-Schneider T., Lauber P., Mishchenko A., Poli E. and Vlad G. 2021 Gyrokinetic investigation of the nonlinear interaction of Alfvén instabilities and energetic particle-driven geodesic acoustic modes *Phys. Plasmas* **28** 072504

[30] Gaffey J.D. 1976 Energetic ion distribution resulting from neutral beam injection in tokamaks *J. Plasma Phys.* **16** 149–69

[31] Mishchenko A., Könies A., Kleiber R. and Cole M. 2014 Pullback transformation in gyrokinetic electromagnetic simulations *Phys. Plasmas* **21** 092110

[32] Mishchenko A. *et al* 2019 Pullback scheme implementation in ORB5 *Comput. Phys. Commun.* **238** 194–202

[33] Vlad G. *et al* 2021 A linear benchmark between HYMAGYC, MEGA and ORB5 codes using the NLED-AUG test case to study Alfvénic modes driven by energetic particles *Nucl. Fusion* **61** 116026

[34] Lauber P. *et al* (The ASDEX Upgrade Team) 2018 Strongly non-linear energetic particle dynamics in ASDEX Up-grade scenarios with core impurity accumulation *Proc. 27th IAEA Fusion Energy IAEA* (Gandhinagar, India, 2018) (https://nucleus.iaea.org/sites/fusionportal/Shared%20Documents/FEC%202018/fec2018-preprints/preprint0319.pdf)

[35] Hawryluk R.J. 1981 An empirical approach to tokamak transport *Physics of Plasmas Close to Thermonuclear Conditions* (Amsterdam: Elsevier) pp 19–46

[36] Fu G.Y. and Van Dam J.W. 1989 Excitation of the toroidicity-induced shear Alfvén eigenmode by fusion alpha particles in an ignited tokamak *Phys. Fluids* B **1** 1949–52

[37] Novikau I. *et al* 2020 Nonlinear dynamics of energetic-particle driven geodesic acoustic modes in ASDEX Upgrade *Phys. Plasmas* **27** 042512

[38] Poloskei P.Z., Papp G., Pokol G., Lauber P. and Horvath L. 2017 Strongly non-linear energetic particle dynamics in ASDEX Upgrade scenarios with core impurity accumulation *Proc. 44th EPS Conf. Plasma Physics* (http://ocs.ciemat.es/EPS2017PAP/pdf/P5.179.pdf)

[39] Fu G.Y. 2008 Energetic-particle-induced geodesic acoustic mode *Phys. Rev. Lett.* **101** 185002

[40] Zonca F. and Chen L. 2008 Radial structures and nonlinear excitation of geodesic acoustic modes *Europhys. Lett.* **83** 35001

[41] Zarzoso D., Biancalani A., Bottino A., Lauber P., Poli E., Girardo J.-B., Garbet X. and Dumont R.J. 2014 Analytic dispersion relation of energetic particle driven geodesic acoustic modes and simulations with NEMORB *Nucl. Fusion* **54** 103006

[42] Zonca F., Chen L., Briguglio S., Fogaccia G., Milovanov A.V., Qiu Z., Vlad G. and Wang X. 2014 Energetic particles

and multi-scale dynamics in fusion plasmas *Plasma Phys. Control. Fusion* **57** 014024
[43] Zonca F., Chen L., Briguglio S., Fogaccia G., Vlad G. and Wang X. 2015 Nonlinear dynamics of phase space zonal structures and energetic particle physics in fusion plasmas *New J. Phys.* **17** 013052
[44] Falessi M.V. and Zonca F. 2019 Transport theory of phase space zonal structures *Phys. Plasmas* **26** 022305
[45] Zonca F., Chen L., Falessi M.V. and Qiu Z. 2021 Nonlinear radial envelope evolution equations and energetic particle transport in tokamak plasmas *J. Phys.: Conf. Ser.* **1785** 012005
[46] Cordey J.G. and Core W.G.F. 1974 Energetic particle distribution in a toroidal plasma with neutral injection heating *Phys. Fluids* **17** 1626–30
[47] Estrada-Mila C., Candy J. and Waltz R.E. 2006 Turbulent transport of alpha particles in reactor plasmas *Phys. Plasmas* **13** 112303
[48] Angioni C. and Peeters A.G. 2008 Gyrokinetic calculations of diffusive and convective transport of α particles with a slowing-down distribution function *Phys. Plasmas* **15** 052307
[49] Di Siena A., Görler T., Doerk H., Bilato R., Citrin J., Johnson T., Schneider M. and Poli E. 2018 Non-Maxwellian fast particle effects in gyrokinetic gene simulations *Phys. Plasmas* **25** 042304
[50] Betti R. and Freidberg J.P. 1992 Stability of Alfvén gap modes in burning plasmas *Phys. Fluids* B **4** 1465–74
[51] Novikau I. *et al* 2021 Implementation of energy transfer technique in ORB5 to study collisionless wave–particle interactions in phase-space *Comput. Phys. Commun.* **262** 107032
[52] Bottino A. and Sonnendrücker E. 2015 Monte Carlo particle-in-cell methods for the simulation of the Vlasov–Maxwell gyrokinetic equations *J. Plasma Phys.* **81** 435810501
[53] Lauber P., Günter S., Könies A. and Pinches S.D. 2007 LIGKA: a linear gyrokinetic code for the description of background kinetic and fast particle effects on the mhd stability in tokamaks *J. Comput. Phys.* **226** 447–65
[54] Rettino B., Hayward-Schneider T., Biancalani A., Bottino A., Lauber P., Chavdarovski I., Vannini F. and Jenko F. 2022 Gyrokinetic modelling of anisotropic energetic particle driven instabilities in tokamak plasmas *Nucl. Fusion* **62** 076027